We are IntechOpen,
the world's leading publisher of
Open Access books
Built by scientists, for scientists

4,800
Open access books available

122,000
International authors and editors

135M
Downloads

Our authors are among the

154
Countries delivered to

TOP 1%
most cited scientists

12.2%
Contributors from top 500 universities

CLARIVATE ANALYTICS
BOOK CITATION INDEX
INDEXED

WEB OF SCIENCE™

Selection of our books indexed in the Book Citation Index
in Web of Science™ Core Collection (BKCI)

Interested in publishing with us?
Contact book.department@intechopen.com

The Physics of High-Efficiency Thin-Film III-V Solar Cells

Roger E. Welser, Ashok K. Sood,

Ramesh B. Laghumavarapu, Diana L. Huffaker,

David M. Wilt, Nibir K. Dhar and Kimberly A. Sablon

Additional information is available at the end of the chapter

1. Introduction

Optically-thin absorber structures represent an interesting class of photovoltaic devices, both in terms of their performance characteristics and the economic advantages of employing thinner semiconductor material layers. This chapter reviews the underlying physics of high-efficiency optically-thin solar cells employing thin-film III-V materials. By combining thin III-V absorber structures with advanced light-trapping structures, single-junction devices can deliver high efficiency performance over a wide range of operating conditions at a fraction of the cost of multi-junction structures. Moreover, by leveraging hot carrier and/or optical up-conversion mechanisms to extend infrared absorption, the power conversion efficiencies in single-junction nano-enhanced solar cells can potentially exceed the Shockley-Queisser limit and outperform multi-junction devices. Experimentally, suppressed radiative recombination and high voltage operation have been observed in step-graded InGaAs quantum well structures. In addition, recent results from a novel InAs/AlAsSb quantum dot structure prove the validity of the intermediate band solar cell approach for infrared up-conversion, and underline the potential of thin-film III-V materials for realizing cost-effective, high-efficiency solar cells.

By minimizing semiconductor material content, optically-thin absorber structures provide a pathway to lower the manufacturing cost of high-performance photovoltaic (PV) devices. Thin-film solar cells are also an attractive source of portable and mobile power, as they can be integrated into flexible, lightweight photovoltaic modules that can operate in both terrestrial and space environments. Several different emerging technologies can be employed to fabricate flexible thin-film PV cells [1-2]. Although the deposition of copper indium gallium diselenide (CIGS) directly onto flexible substrates offers some advantages in terms of ease of manufacturing, the epitaxial lift-off (ELO) of III-V devices can provide much higher efficiency performance.

By stacking multiple p-n junctions of different III-V semiconductor materials into one two-terminal device, multi-junction solar cells have achieved record-high efficiency at converting solar power into electrical power. Under air mass zero (AM0) spectral conditions found in space, InGaP/GaAs/InGaAs inverted metamorphic (IMM) cells have been demonstrated with efficiencies in excess of 32% [3-4]. Even higher efficiencies exceeding 35% have been achieved under an air mass spectrum (AM1.5) typically used to characterize terrestrial performance [5]. However, changes in the solar spectrum can dramatically degrade the performance of multi-junction devices – changes that occur naturally throughout the day, from season to season, and from location to location as sunlight passes through the earth's atmosphere. As illustrated in Figure 1, the efficiency of a multi-junction device will decrease by more than a factor of two under higher air mass spectra. This reduction in efficiency is due to a decrease in the current output of the series-connected multi-junction device, which is limited by the subcell generating the least amount of photocurrent. Series-connected multi-junction cells can also degrade more rapidly than single-junction III-V cells upon irradiation, particularly as the current output of the limiting subcell fails. Moreover, multi-junction III-V cells require thick, complex epitaxial layers and are therefore inherently expensive to manufacture. Thus the inconsistent performance under changing environmental conditions and high manufacturing costs of multi-junction III-V cells severely hamper the application of this established high-efficiency technology.
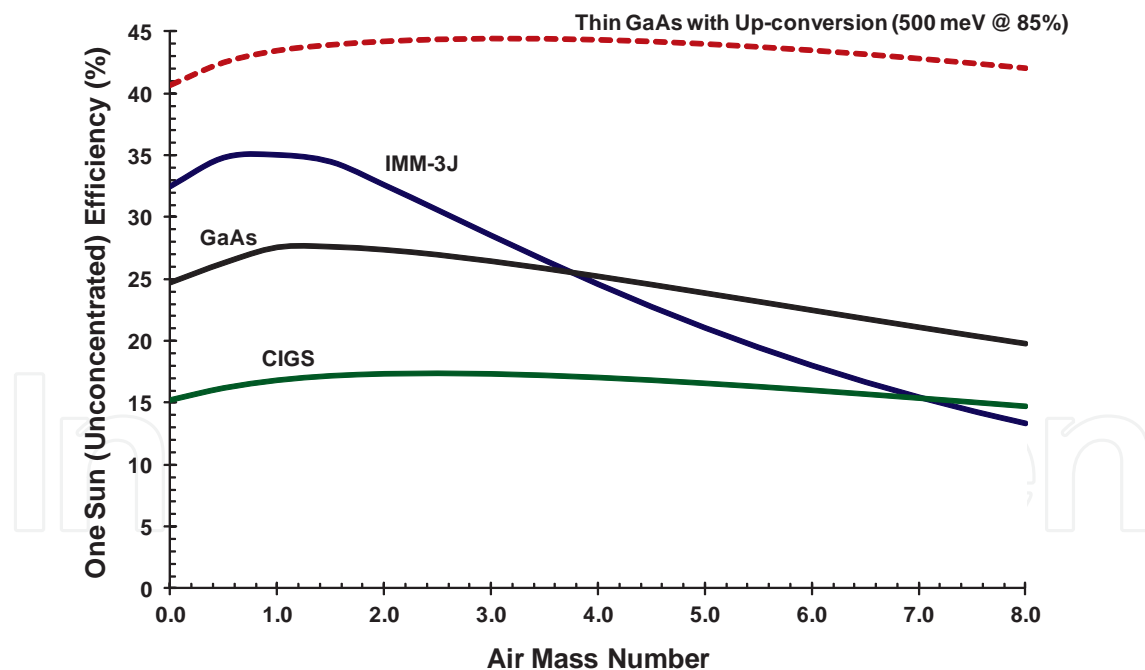

Figure 1. Projected un-concentrated efficiency versus air mass spectrum for several different types of solar cell structures, including a high-performance IMM triple-junction III-V structure, a single-junction CIGS cell, and a single-junction GaAs solar cell. Also shown is the theoretical performance of a thin GaAs-based device incorporating up-converting and light-trapping structures to harness a notable fraction of the available low energy photons. The calculations assume a Bird – Riordan model of the air mass spectrums and realistic spectral response and dark diode characteristics, as detailed in reference [6].

Thin-film single-junction III-V cells can potentially address the performance and cost limitations of multi-junction devices. By avoiding current matching constraints, single-junction structures can offer a more robust performance than multi-junction devices [6]. The efficiency of established single-junction CIGS and GaAs cell technologies is more stable to changes in the incident spectrum, and can actually outperform III-V multi-junction structures under higher air mass spectrums, as depicted in Figure 1. Moreover, the efficiency of single-junction III-V cells can be dramatically increased by employing additional structures that leverage optical up-conversion and/or hot carrier effects. Theoretically, both up-conversion and hot carrier mechanisms have been projected to increase the limiting one-sun efficiency of single-junction photovoltaic devices to over 50% [7-8]. By combining thin III-V absorber structures with advanced light-trapping structures, nano-enhanced III-V single-junction devices can potentially deliver high efficiency performance in a flexible format at a fraction of the cost of multi-junction structures. As illustrated in Figure 1, efficiencies of more than 40% over a wide range of spectrums are projected for an optically-thin GaAs-based device that can harness 85% of the infrared photons falling within 500 meV of the GaAs band edge [6].

In this chapter, the theoretical performance of optically-thin solar cells is first described using a generalized detailed balance model, specifically adapted for nano-enhanced absorbers. This model is then employed to describe the impact of both absorber thickness and effective optical path length on the performance of III-V photovoltaic devices, using data from GaAs-based structures to validate the approach. In later sections, recent experimental work focused on reducing the diode dark current (and hence increasing the operating voltage) and boosting the current output of nano-enhanced III-V solar cells is summarized. In particular, the combination of a thin optical absorber and advanced light trapping structures is shown to provide a means to increase the voltage of operation while maintaining current output in photovoltaic devices. However, if the absorber thickness is reduced too far, two-dimensional carrier confinement effects will in essence enhance radiative recombination and negate the voltage benefits of thin-absorber cells. In addition, optical losses in the high-doped contact layers and surface regions can limit some of the benefits of light-trapping on voltage in thin-absorber structures. There are, however, several other mechanisms for reducing radiative emissions in photovoltaic devices. For example, radiative emissions can be minimized and voltage enhanced by embedding thin-absorbers in lower refractive index material or employing step-graded structures to harness hot carrier effects. Finally, infrared up-conversion provides a pathway to enhance current output and thus increase efficiency.

2. Generalized detailed balance model applied to optically-thin nano-enhanced devices

The concept of detailed balance is often used to estimate the limiting efficiency of ideal photovoltaic devices. Since its introduction by Shockley-Queisser, detailed balance calculations have been generalized to include a continuous absorbance function and a variety of different cell geometries [9-11]. More recently, detailed balance concepts have been further generalized and applied to the analysis of experimental results from several different types of

functional photovoltaic devices [12-14]. In this section, a generalized detailed balance model is applied to optically-thin nano-enhanced photovoltaic absorber structures. A device geometry with negligible photon recycling is considered the starting point for the discussion because of the reduced absorption inherent to optically-thin structures. Experimental dark current and external quantum efficiency characteristics from a high-voltage InGaAs quantum well structure are then analyzed within the framework of this generalized detailed balance model.

By extending detailed balance concepts to include both carrier generation and carrier transport properties, Kirchartz and Rau have demonstrated that the photovoltaic external quantum efficiency, Q_e (E), measured at normal incidence, can be related to the radiative dark current and luminescent characteristics of photovoltaic (PV) and light emitting diode (LED) devices [13]. The radiative dark current (J_{rad}) follows an n=1 voltage dependence, β (V) = exp(qV/kT) – 1, that will fundamentally limit the operating voltage of a photovoltaic device, and that can be related to the experimentally measured external quantum efficiency:

$$J_{rad} = q \int Q_e(E) \, \phi_{bb}(E) \, \beta(V) \, dE \tag{1}$$

where q is the elementary charge, V is the applied bias voltage, and kT is the thermal energy. The relevant blackbody spectral photon density spectrum, ϕ_{bb} (E), in Equation (1) is contingent upon the cell geometry, but can be generalized here with the introduction of a dark current factor (F_{dc}) to characterize, among other things, the overall effective etendue of the photovoltaic device, such that:

$$\phi_{bb}(E) = \left(2 \, F_{dc} \, / \, h^3 c^2\right) E^2 \, / (\exp(E/kT) - 1) \tag{2}$$

In many detailed balance calculations, F_{dc} is often assumed to be as low as π, corresponding to the limit in which emitted photons are reabsorbed after perfect reflection off the back surface or total internal reflection off the front surface. However, such photon recycling effects, which effectively restrict the angular emissions of the device, may become negligible in optically-thin structures with low reflectance surfaces and/or high absorbing contact layers. In this limit of negligible re-absorption:

$$F_{dc} = 2 \, \pi \, n_b^2 \tag{3}$$

where n_b is the refractive index of the barrier material surrounding the optically-thin absorber.

The external quantum efficiency of a photovoltaic device, Q_e (E), is also related to the short circuit current density (J_{sc}) via:

$$J_{sc} = q \int U_c(E) \, Q_e(E) \, \phi_{sun}(E) \, dE \tag{4}$$

where ϕ_{sun} (E) is the incident solar spectrum and U_c (E) is a correction factor to the photocurrent introduced here in order to account for optical up-conversion effects [15]. In

conventional PV devices, U_c (E) = 1. However, in some devices, including optically-thin nano-enhanced absorber structures, the presence of low-energy photons can enhance carrier generation beyond that measured in a typical photovoltaic external quantum efficiency measurement [16-18], resulting in an effective enhancement in the incident solar spectrum such that U_c (E) > 1.

The validity of the generalized detailed balance model for optically-thin photovoltaic devices described above has been confirmed by analyzing experimental results from a high-voltage InGaAs quantum well solar cell. The measured external quantum efficiency and current-voltage characteristics from a high-voltage GaAs-based diode with a single nearly-square 15 nm InGaAs well embedded within the junction depletion region are summarized in Figure 2. The baseline diode consists of an extended p-type wide band gap emitter, which minimizes non-radiative recombination, and a relatively thin (0.5 μm) GaAs base layer, similar to the high-voltage InGaAs well structures described in reference [19]. As-grown wafers were quartered and 0.25 cm^2 thin-film cells were fabricated using a substrate removal process at MicroLink Devices [20]. The measured external quantum efficiency characteristics summarized in Figure 2 (a) were taken from a cell employing a low reflectance two-layer anti-reflectance coating on the front surface and an absorbing Ge-based back metallization. Small, simple mesa test devices were also fabricated via standard wet etch chemistry and photolithography on a second quarter piece of the same wafer. For the dark I-V measurements reported in Figure 2 (b), a test structure consisting of a device with a junction area of 200 μm x 270 μm has been employed.

The measured dark current in Figure 2 (b) exhibits a non-ideal voltage dependence at lower bias, presumably due to non-radiative recombination within the depletion region. However, the voltage dependence of the dark current approaches unity as the bias approaches 1 V. Quantitatively, the measured dark current at higher bias nearly matches the radiative dark current calculated from Equations (1) – (3), assuming T = 25°C, n_b = 3.5 (refractive index of the GaAs surrounding the well), and the measured external quantum efficiency shown in Figure 2 (a). While the calculated n=1 component of the dark current shown in Figure 2 (b) assumes negligible re-absorption ($F_{dc} = 2\pi n_b^2$), we note that the dark current factor can be generalized further to account for non-radiative and non-equilibrium effects. Non-radiative recombination will result in higher effective F_{dc} values that can also vary with voltage if recombination occurs within the junction depletion region. On the other hand, lower F_{dc} values could be obtained if the overall angular emissions of the device are restricted, for example via photon recycling, or through non-equilibrium effects such as hot carrier extraction. Finally, we note that misleadingly high F_{dc} values could be obtained if the falloff in Q_e (E) is not accurately measured at longer wavelengths, as emissions from the Urbach tail region can have a significant impact on the dark current, as will be discussed in later sections.
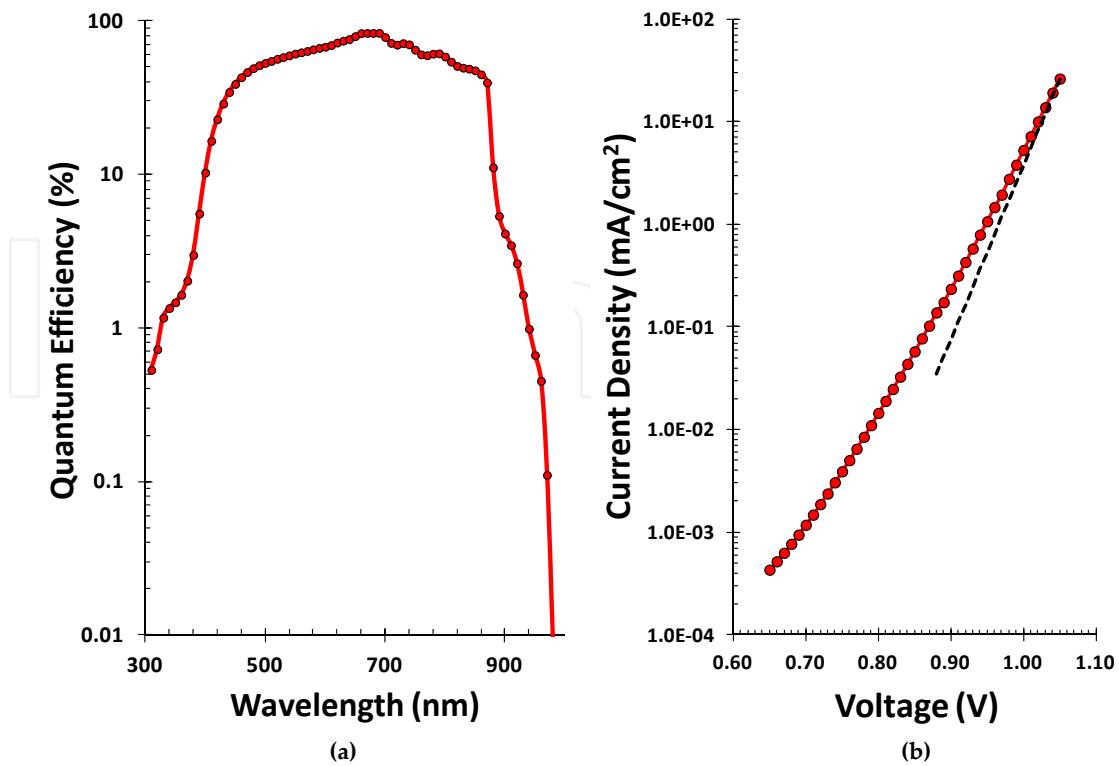
Figure 2. External quantum efficiency spectra (a) and dark current-voltage measurements (b) from a high voltage In-GaAs quantum well solar cell structure employing an extended wide band-gap AlGaAs/InGaP emitter heterojunction. The dashed line in (b) is the calculated J_{rad} from equations (1) – (3) using the measured Q_e (E).

3. Dependence of radiative dark current on absorber thickness

Like conventional photovoltaic devices, the output voltage of optically-thin solar cells is governed by the underlying dark current. The dark current of typical III-V semiconductor diodes is composed of several different components involving both radiative and non-radiative processes. Non-radiative dark current processes can follow either an n=2 or n=1 voltage dependence, contingent upon the location of the recombination. Non-radiative defects within the junction depletion region contribute to the n=2 space charge recombination component of the dark current, while non-radiative defects in the quasi-neutral regions of the device contribute to the n=1 component. Radiative processes also follow an n=1 voltage dependence, and as discussed in the previous section, will ultimately limit the voltage performance of the best photovoltaic devices. In this section, the impact of absorber layer thickness on the radiative dark current is detailed after making some simplifying assumptions regarding absorption processes in GaAs-based devices.

In a previous section, we summarized how detailed balance considerations can be used to relate the radiative dark current to the external quantum efficiency – e.g. Equation (1). The external quantum efficiency is in turn proportional to the effective absorber layer width (W_{eff}) and the absorption coefficient α (E):

$$Q_e(E) = C(E)\,\alpha(E)\,W_{eff} \tag{5}$$

where C (E) is a correction factor which accounts for loss mechanisms, such as reflections off the front surface and photogenerated carrier recombination prior to collection. While the absorption coefficient of GaAs is arguably the most well-known of all the III-V compounds, the reported values can vary significantly with doping, particularly at energies close to and below the band gap. In this section, the GaAs absorption coefficient is modeled using a piecewise continuous function as described in Miller *et al.* [21] but calibrated using the experimental data from Kurtz *et al.* [22], as shown in Figure 3 (a).
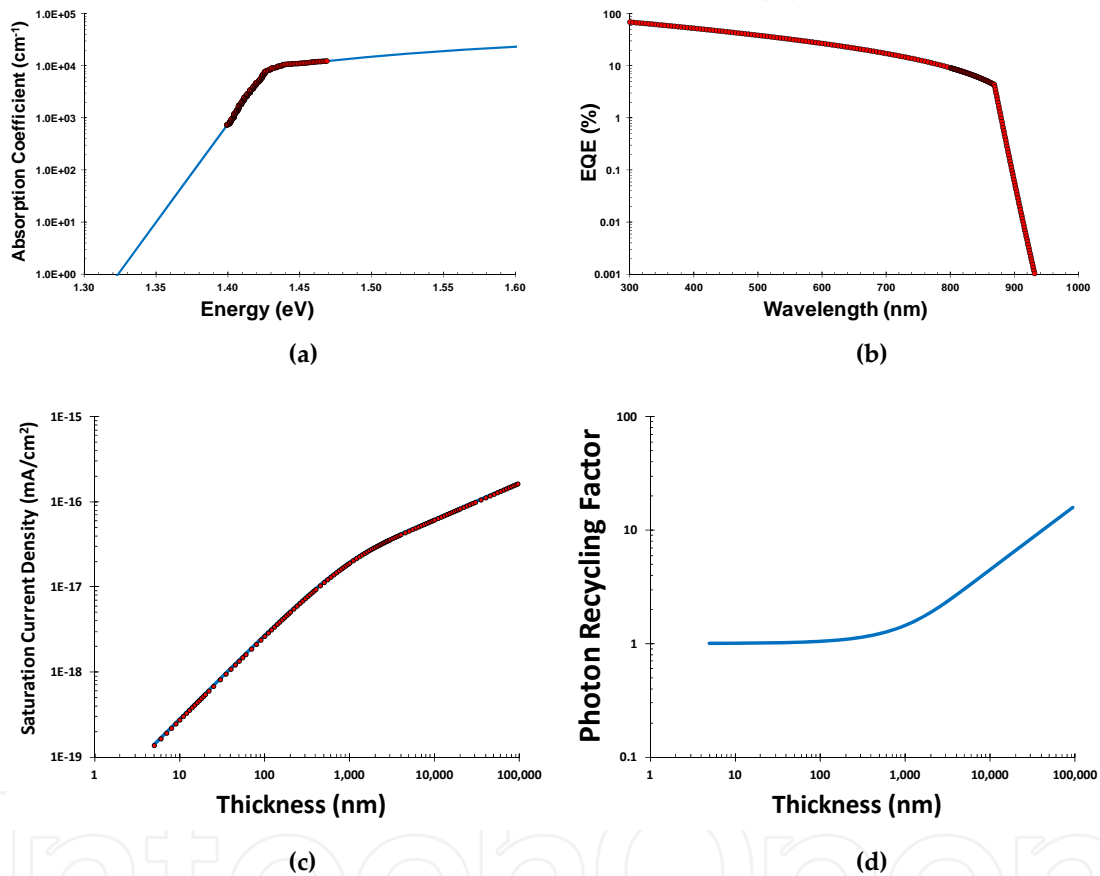

Figure 3. (a) Modeled (line) and measured (circles) absorption spectra of GaAs; (b) modeled external quantum efficiency spectra for a 50 nm GaAs absorber; (c) dependence of the radiative saturation dark current as a function of absorber layer thickness as calculated (circles) from detailed balance considerations and fit (line) to Equation (6); and (d) photon recycling factor as a function of absorber thickness, derived from the fit to Equation (6).

In the limit of negligible photon recycling, the effective absorber layer width can be equated to the physical absorber layer width ($W_{eff} = W_p$). Furthermore, in ideal structures, reflection losses are minimized and all of the absorbed photons are collected, e.g. C (E) = 1. With these simplifying assumptions, the external quantum efficiency can be calculated from equation (5) for any given thickness of an ideal GaAs absorber. For example, Figure 3 (b) depicts the calculated external quantum efficiency spectrum of a 50 nm GaAs layer. The Q_e (E) generated from Equation (5) can then be combined with equations (1) – (3) to calculate the dependence

of saturated radiative dark current on absorber thickness for GaAs, as summarized in Figure 3 (c). Clearly the radiative dark current can be reduced, and the operating voltage enhanced, by minimizing the absorber layer thickness.

Radiative recombination can also be described mechanistically in terms of carrier recombination via the use of a radiative recombination coefficient. With this mechanist approach, the radiative saturation current density ($J_{o1,rad}$) can be related to the intrinsic carrier density (n_i) and the physical absorber layer thickness (W_p) via a three-dimensional radiative recombination coefficient (B_{3D}):

$$J_{o1,rad} = q\ n_i^2\ (B_{3D}/\phi_r)\ W_p \tag{6}$$

where ϕ_r is Asbeck's photon recycling co-factor [23-24]. Figure 3 (d) summarizes the dependence of ϕ_r on thickness, as inferred from fitting Equation (6) to the radiative dark current derived from detailed balance calculations as described above and summarized in Figure 3 (c). Assuming $n_i = 2.1 \times 10^6$ cm^{-3}, a typical value quoted for GaAs, the fit also implies $B_{3D} = 3.9 \times 10^{-10}$ cm^3/s, reasonably in-line with previous estimates of the radiative recombination coefficient in GaAs [23].

4. Transition from 3D to 2D carrier confinement

Nano-enhanced III-V absorbers are a specific example of optically-thin photovoltaic device structures that are being investigated as a pathway to extend infrared absorption and increase photovoltaic power conversion efficiency. In a typical III-V nano-enhanced solar cell, quantum well and/or quantum dot layers are added to the depletion region of a PIN diode. In principle, the addition of narrow band gap material to the diode structure is expected to result in an increase in the fundamental radiative dark current. In practice, non-radiative recombination both in the narrow band gap material and underlying baseline diode often obscures the radiative dark current. However, nano-enhanced absorber structures with a novel material structure have recently achieved ultra-low dark currents by employing advanced band gap engineering to suppress non-radiative recombination and expose the limiting radiative component of the dark current [19]. As the thickness of the absorber layer decreases, quantum confinement effects can begin to play a role. In this quantum confinement limit, the variation of the radiative dark current with thickness will deviate from that implied in Equation (6), as derived in the previous section.

In this section, we describe the saturation in radiative recombination with decreasing well thickness observed in both photoluminescence and dark current measurements on high-voltage, single InGaAs well structures. The observed saturation in PL intensity and radiative dark current is consistent with a transition from a three-dimensional (3D) to a two-dimensional (2D) density of states as quantum confinement effects increase with decreasing well thickness. The dependence of the radiative dark current on well thickness is described mechanistically in terms of a transition from 3D to 2D carrier recombination.

Figure 4 compares the photoluminescence spectra and diode dark currents from a set of single, square InGaAs well structures with varying well thickness but the same effective well energy. These InGaAs quantum well structures have been synthesized on semi-insulating GaAs substrates via metal-organic chemical vapor deposition (MOCVD). To minimize the diode dark current, an extended wide band gap emitter heterojunction structure has been employed, consisting of wide energy-gap InGaP and AlGaAs materials in the emitter and in the depletion region adjacent to the emitter [19]. To ensure that photogenerated carriers can overcome potential energy barriers via field-assisted thermionic emission, the InGaAs quantum wells and the transitions to higher energy-gap materials are located within the built-in field of the junction depletion region [25].

The as-grown samples have been characterized by photoluminescence (PL) measurements generated with excitation from a 785 nm laser source. In Figure 4 (a), the PL intensity measured on each sample has been normalized to the peak GaAs base layer emissions near 1.42 eV. The PL emission peak from the InGaAs well is a function of both the well composition and thickness. In the set of structures discussed in this section, the indium composition in the well is higher in the thinner wells in order to maintain a peak PL emission near 1.32 eV. Interestingly, the relative PL intensity from the InGaAs layer clearly decreases as the well thickness decreases from 30 nm to 15 nm, but is only marginally lower for the structure with the thinnest well (2.5 nm).

The wafers were quartered after the PL measurements, and standard wet etch chemistry and photolithography were employed to define simple mesa test devices with junction areas as small as 75 μm x 75 μm. These devices were then characterized via illuminated current versus voltage, capacitance versus voltage, and dark current versus voltage measurements. For dark I-V measurements shown in Figure 4 (b), a test structure consisting of a device with a junction area of 200 μm x 270 μm has been employed. While some sample-to-sample scatter in the n=2 space charge recombination component of the dark current is observed, the magnitude of n=1 component of the measured dark current mimics the behavior of the relative PL intensity emitted by the InGaAs wells. Specifically, the n=1 component decreases with well thickness from 30 nm to 15 nm, but the 2.5 nm sample has a dark current that is nearly indistinguishable from the 15 nm sample. This observed near saturation in PL intensity and radiative dark current is consistent with a transition from a three-dimensional (3D) to a two-dimensional (2D) density of states as quantum confinement effects increase with decreasing well thickness.

Figure 5 compares the reverse saturation radiative current density, as derived by scaling the integrated PL spectra in Figure 4 (a), to the n=1 reverse saturation current density extracted directly from the measured dark diode current in Figure 4 (b). The comparison in Figure 5 indicates a very close correlation between the photoluminescence and dark current measurements in this sample set. By relating the radiative recombination rate to the intrinsic carrier density (n_i) via a bulk three-dimensional radiative recombination coefficient (B_{3D}), the radiative dark current in an optically thin absorber has previously been expressed in terms of the physical absorber layer thickness (W_p) – e.g. Equation (6). However, radiative emissions from quantum-confined structures can be more appropriately described in terms of a two-dimensional radiative recombination coefficient (B_{2D}) [26]. In particular, the rate of radiative recombination in a quantum-confined layer is proportional to the product of the electron and hole

densities within the quantum well. In the limit of evenly emitting wells in which the effective carrier densities are the same within each well, the radiative current density generated by a multiple quantum well structure can be expressed as:

$$J_{o1,rad} = q \, n_{qw} \, p_{qw} \, B_{2D} M_{qw} \tag{7}$$

where n_{qw} and p_{qw} are the effective quantum well electron and hole densities per unit area at zero bias and M_{qw} is the number of wells in the structure ($M_{qw} = 1$ in the set considered here). For any given effective well energy, equation (7) implies that the radiative component of the dark current will scale with the number of wells, independent of well thickness.
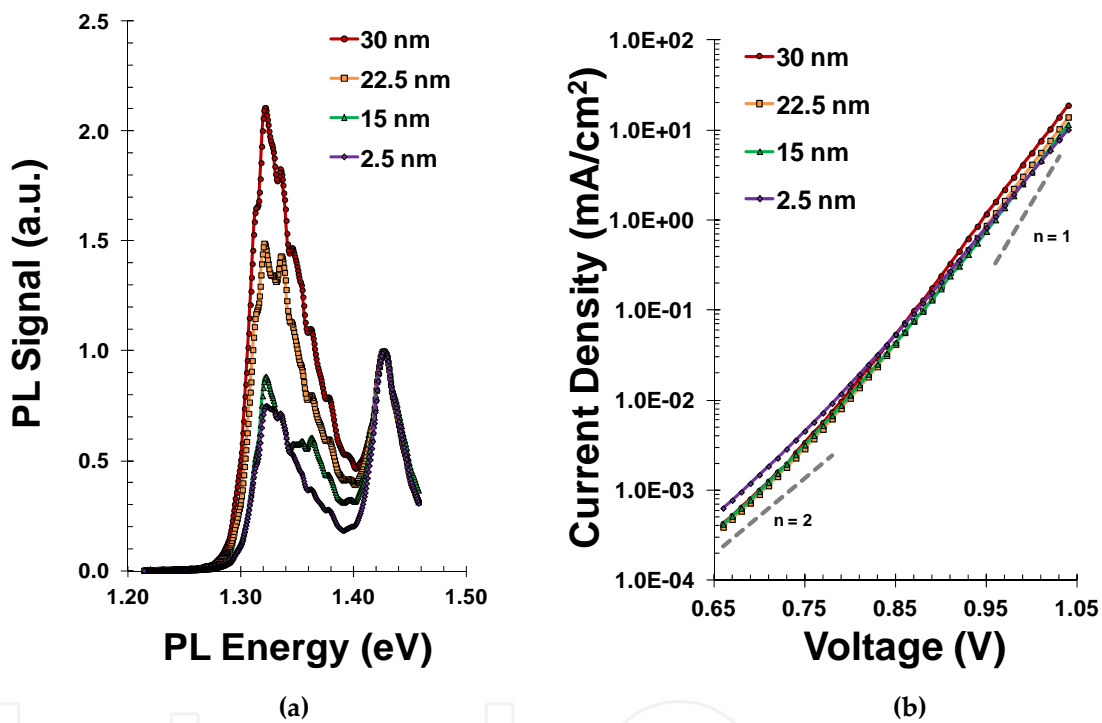
Figure 4. Normalized photoluminescence spectra (a) and dark current-voltage measurements (b) from a set of high-voltage InGaAs quantum well solar cell structures, all emitting at approximately 1.325 eV but with varying well thickness.

In Figure 5, the reverse saturation current density values inferred from both the dark diode current and photoluminescence measurements are compared to calculations using Equations (6) and (7). For the thicker samples, the variation in $J_{o1,rad}$ with absorber layer thickness is well fit by a 3D representation of the carrier recombination, as given by Equation (6), assuming the radiative recombination coefficient is independent of indium composition (B_{3D} = 3.9 x 10^{-10} cm^3/s) and that the intrinsic carrier combination scales inversely with the effective energy gap ($n_i = (N_c N_v)^{1/2} \exp(-E_g/2kT) = 1.57$ x 10^7 cm^{-3}). On the other hand, for the thinner samples, the variation in $J_{o1,rad}$ with absorber layer thickness is well fit by a 2D representation of the carrier recombination as given by Equation (4), assuming $n_{qw} = p_{qw} = 0.37$ cm^{-2} and $B_{2D} = 1.3$ x 10^{-3} cm^2/s.
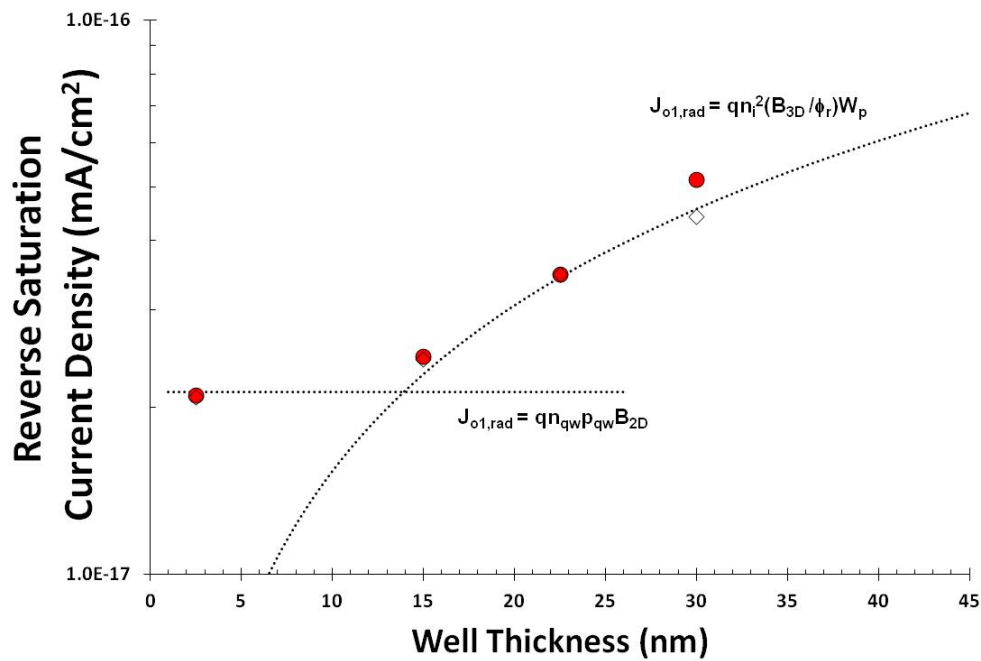
Figure 5. Reverse saturation current density of the n=1 component of the diode current as derived from the measured dark diode current (solid circles) and calculated from the measured PL spectra (open diamonds). Also shown is the expected variation in the radiative dark current in the 3D and 2D regimes using Equations (6) and (7).

5. Impact of enhanced optical path length

The application of light trapping structures to thin-film devices provides a means to both further suppress the radiative dark current via photon recycling and increase the current output via enhanced optical path lengths within the thin absorber structure. Figure 6 summarizes the current-voltage characteristics of a simple example of an optically-thin absorber structure employing a reflective back contact [6]. This uncoated test device employs a 30 nm GaAs absorber embedded within a wider energy-gap InGaP/AlGaAs heterojunction, and has been fabricated into a thin-film device using an epitaxial liftoff process at MicroLink Devices [20]. Record-low dark current characteristics for a GaAs-based device have resulted in an ultra-high open circuit voltage (V_{oc}) of 1.122 V at a short circuit current density (J_{sc}) of 14.7 mA/cm^2.

Equation (6) can be employed to estimate the expected impact of enhanced optical path length on the radiative dark current of a GaAs-based device. In particular, Figure 7 compares the calculated dependence of the radiative n=1 saturation current density as a function of absorber thickness for four different structures with varying optical path length (OPL) enhancements. Because photon emissions are omnidirectional in nature, the OPL enhancements assumed in Figure 7 represent angle averaged values. For these calculations, we further assume that $B = 3.9 \times 10^{-10}$ cm^3/s, $n_i = 2.1 \times 10^6$ cm^{-3}, and that self- absorption effects – see ϕ_r dependence on thickness shown in Figure 3 (d) – scale with the OPL factor. Enhancements in the OPL due to reflections off the front and back surfaces of the device can result in the re-absorption of emitted

photons and thus a significant increase of self-absorption effects, particularly in thicker absorber structures.
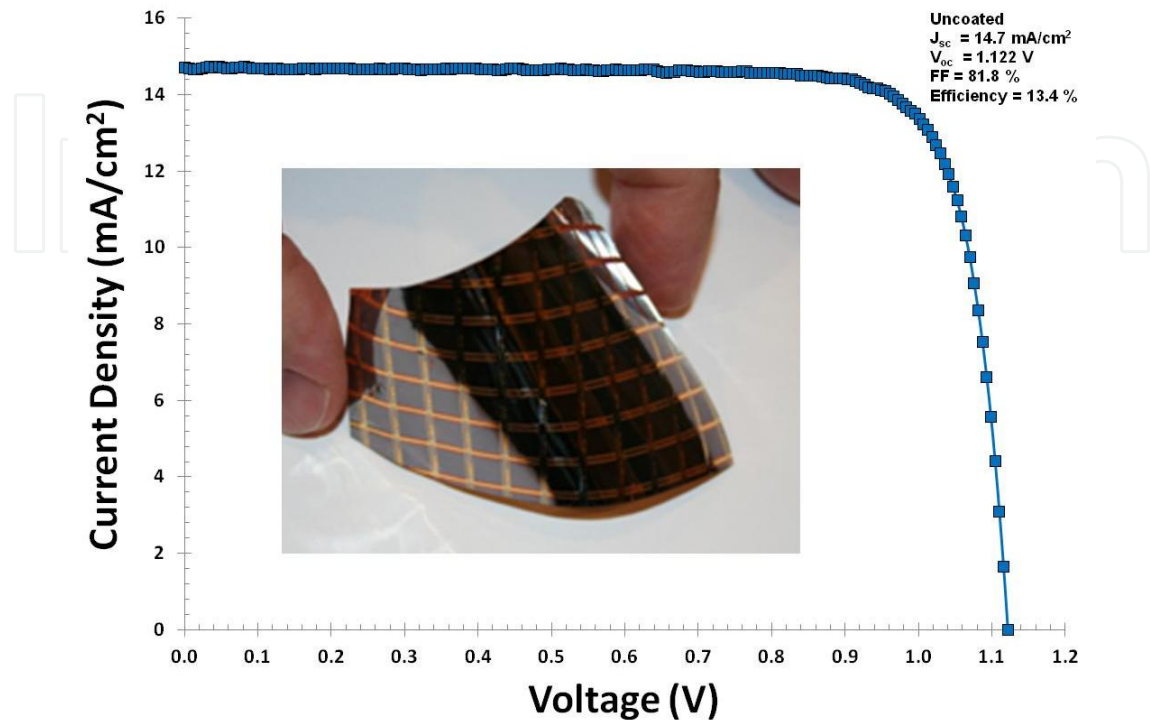

Figure 6. Illuminated current-voltage characteristics from a small area (0.25 cm²), optically-thin GaAs test device fabricated via epitaxial liftoff [19]. An optical photograph of the flexible test cells is shown inset.

For thin absorbers, such as the test device summarized in Figure 6, the impact of light trapping on radiative dark current is relatively small. However, the impact of light trapping on the short circuit current of thin-absorber structures can be quite significant. Figure 8 highlights the dependence of the short circuit current density on both the physical absorber layer thickness and the effective optical thickness due to enhancements in the optical path length. The OPL enhancements shown in Figure 8, unlike Figure 7, are not angle averaged but instead describe the average path length of normal incident photons. For these calculations, the GaAs absorption coefficient was modeled using a piecewise continuous function described in Miller *et al.* [21] but calibrated using the experimental data from Kurtz *et al.* [22], as shown earlier in Figure 3 (a). After accounting for reflection off the front surface of an uncoated device (R ~ 35%), it was further assumed that all absorbed incident low energy photons with wavelengths greater than 715 nm generated collectable electron-hole pairs. Higher energy photons are assumed to be absorbed in a wider energy gap matrix surrounding the GaAs layer, providing 13.1 mA/cm² of current under simulated AM1.5 illumination. The effective thickness in Equation (5) was then assumed to be the product of the physical thickness and the OPL factor. As seen in Figure 7, the application of light trapping structures which can enhance the optical path length of incident photons is projected to have a significant impact on the current output of thin absorber structures, but has minimal impact on thicker absorber structures.
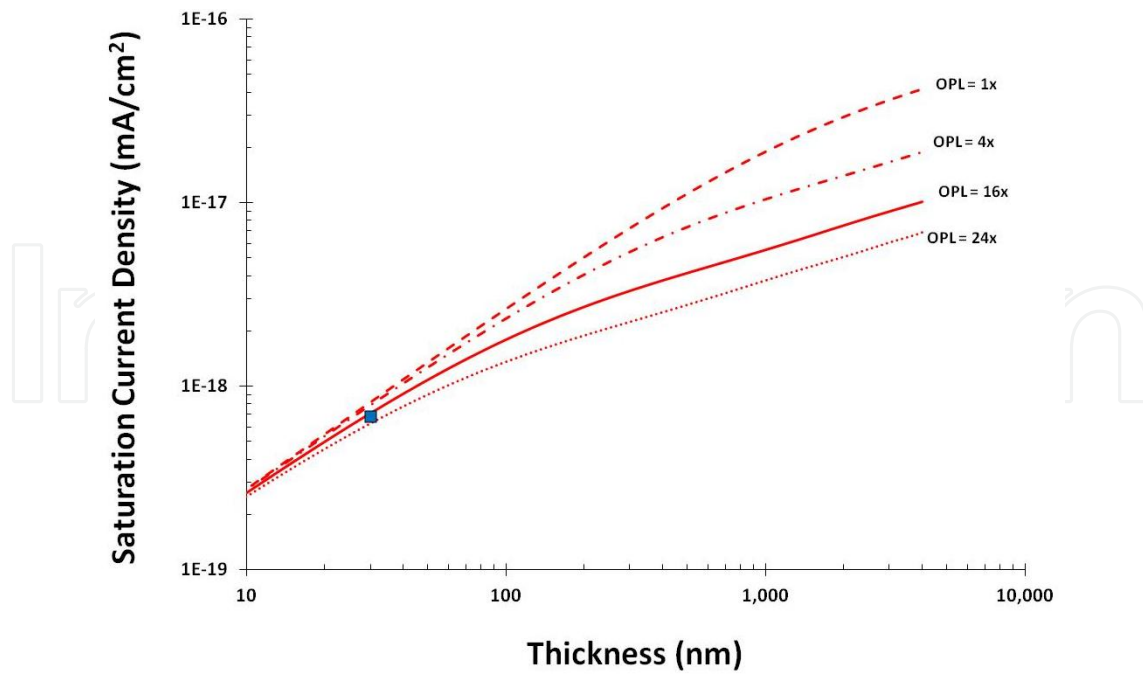
Figure 7. Projected dependence of the radiative saturation dark current as a function of GaAs absorber layer thickness assuming four different structures with varying degrees of light trapping, resulting in optical path length enhancements of 1x, 4x, 16x, and 24x. Also shown is the n=1 saturation dark current extracted from measurements on the optically-thin GaAs test device summarized in Figure 6 and described in more detail in reference [6].
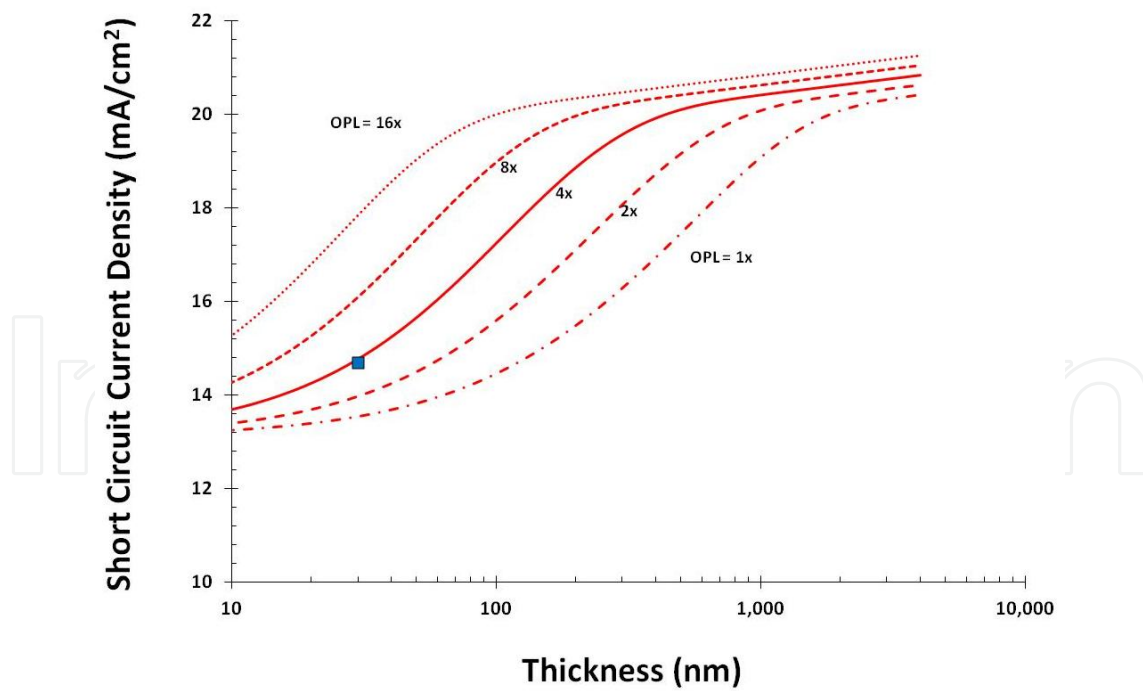

Figure 8. Projected dependence of the uncoated short circuit current as a function of GaAs absorber layer thickness under AM 1.5 illumination, assuming five different structures with varying degrees of light trapping, resulting in optical path length enhancements of 1x, 2x, 4x, 8x, and 16x. Also shown is the short circuit current density measured on the optically-thin GaAs test structure characterized in Figure 6 and described in more detail in reference [6].

6. High-voltage nano-enhanced devices with suppressed radiative recombination

In the last section, we saw that light trapping is not a particularly effective means to reduce the radiative dark current of optically-thin absorber structures. However, recent experimental work indicates that it may be possible to reduce radiative recombination in thin absorber structures by manipulating the compositional profile of quantum well absorbers [19]. In particular, a compositional step-grade design has been experimentally observed to enhance the performance of high-voltage InGaAs quantum well solar cells by reducing the overall diode dark current. A comparison of square and step-graded well structures with varying well thickness but comparable well emission energy suggests a 2x reduction in the radiative recombination coefficient. Theoretically, we will show that reducing either the Urbach tail or the refractive index environment can result in a notable reduction in the radiative dark current of optically-thin structures. In addition, non-equilibrium effects, partially hot-carrier effects, can lead to even more substantial reductions in the radiative dark current.

By embedding narrow energy-gap wells within a wide energy-gap matrix, quantum well solar cells seek to harness a wide spectrum of photons at high voltages in a single-junction device. Quantum well solar cells have the potential to deliver ultra-high efficiency over a wide range of operating conditions, avoiding the limitations of current matching inherent in multi-junction devices. Over the years, quantum well solar cells have been fabricated using a variety of different material systems, and the basic concept has been extended to include quantum dot absorber structures [27-29]. Clear enhancements in the infrared spectral response have been experimentally observed in both quantum well and quantum dot solar cells. Recently, GaAs-based quantum well solar cells with a novel material structure which minimizes non-radiative recombination have also achieved record-high open circuit voltages, in some cases exceeding 1 V at one-sun bias levels [19,30]. In this section, we detail the additional performance benefits resulting from the use of compositionally step-graded InGaAs well designs.

Figure 9 compares external quantum efficiency as derived from measured photoluminescence (PL) spectra and dark diode current-voltage characteristics from a single square InGaAs well photovoltaic device to a similar structure employing a compositionally step-graded well design. The baseline diode consists of an extended p-type wide band gap emitter, which minimizes non-radiative recombination, and a relatively thin (0.5 μm) GaAs base layer, synthesized on semi-insulating GaAs substrates via metal-organic chemical vapor deposition (MOCVD) [19]. In each structure the well is placed within the junction depletion region, as photogenerated carriers can then escape from the well via field-assisted thermionic emission [25]. A comparison of the simplified band structures of the square and step-graded wells is illustrated in Figure 10.

The indium content of the square and step-graded well structures compared in Figure 9 has been tuned to yield a nearly identical peak PL energy of approximately 1.325 eV. As a result, the forward emission and carrier collection characteristics are quite similar. However, the measured dark diode characteristics of the step-graded structure are notably lower than the square structure, with fits of the n=1 component yielding a factor of 2x reduction in the reverse

saturation current density. These results imply that the use of a composition step-graded profile in the quantum well results in a 2x reduction in the radiative recombination coefficient.

There are several possible mechanisms by which a step-graded well profile or other device designs may reduce the radiative recombination coefficient, and thus enhance the limiting operating voltage of photovoltaic devices. For example, any shifts in the absorption profile, and in particular the sub-band gap (e.g. Urbach tail) region, can impact radiative emissions. Figure 11 compares the calculated reverse saturation current density assuming two different Urbach tail energies. As in earlier sections, the absorption spectrum is modeled using a piecewise continuous function [21]. The absorption spectrum is then used to generate an external quantum efficiency spectrum, which is in turn used to calculate the radiative dark current based upon detailed balance concepts – e.g. Equations (5) and (1). Reducing the activation energy which describes the sub-bandgap absorption profile results in a reduction in the radiative dark current, but more so in thicker absorbers. Altering in the Urbach tail absorption characteristics may thus provide some benefits, but seems unlikely to account for the 2x reduction in the radiative recombination B-coefficient observed in thin step-graded well structures.
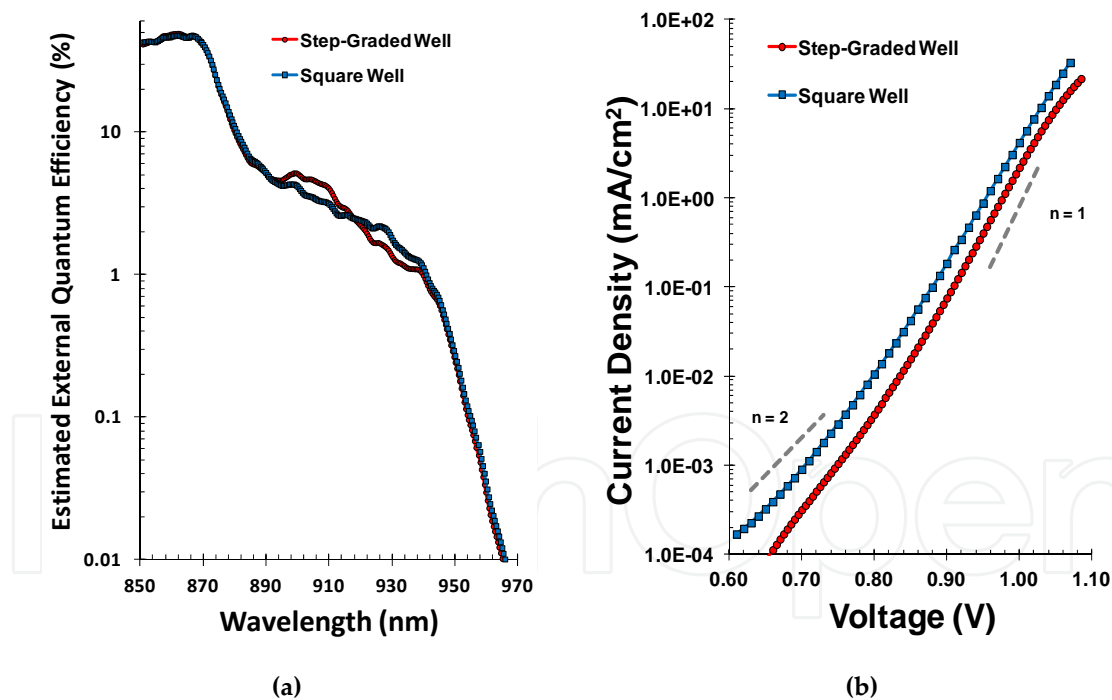

(a)

(b)

Figure 9. Estimated external quantum efficiency (a) and dark current-voltage measurements (b) from two high-voltage InGaAs quantum well structures, one employing a square well and the other a compositionally step-graded well. The external quantum efficiency was estimated from PL measurements assuming a reciprocity relationship between spectral response characteristics and luminescent emissions in PV and LED devices [12]. The dark current was measured on mesa test structures with a junction area of 500 μm x 500 μm fabricated via standard photolithography and wet etch chemistry. The dashed lines depict the slope of ideal n=1 and n=2 components of the dark current.
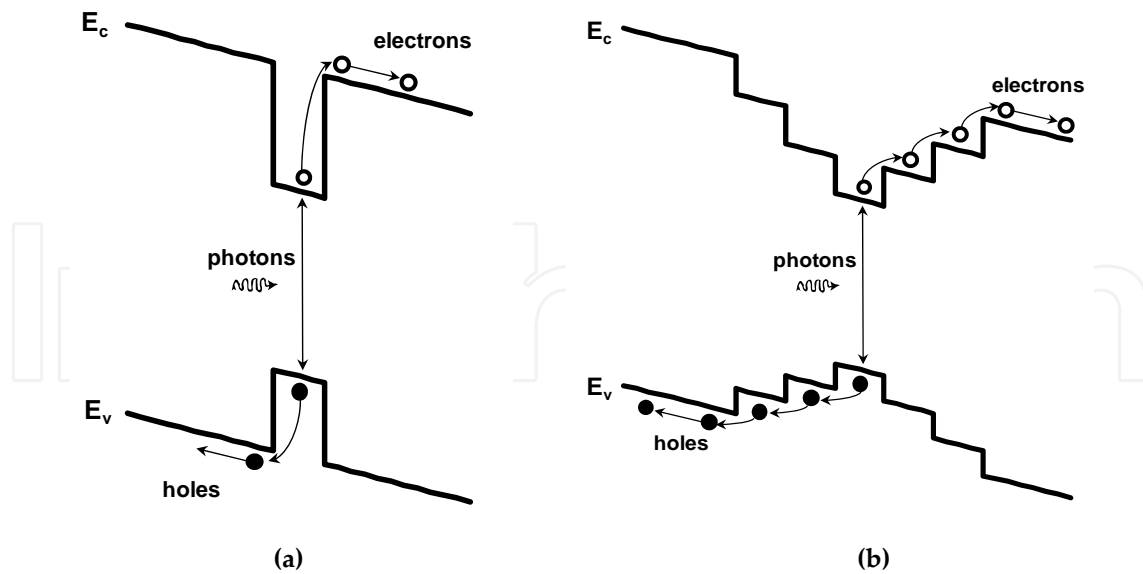
Figure 10. Simplified band structures of the (a) square and (b) step-graded well structures employed in the Figure 9 comparison, illustrating the field-assisted photogenerated carrier escape processes.
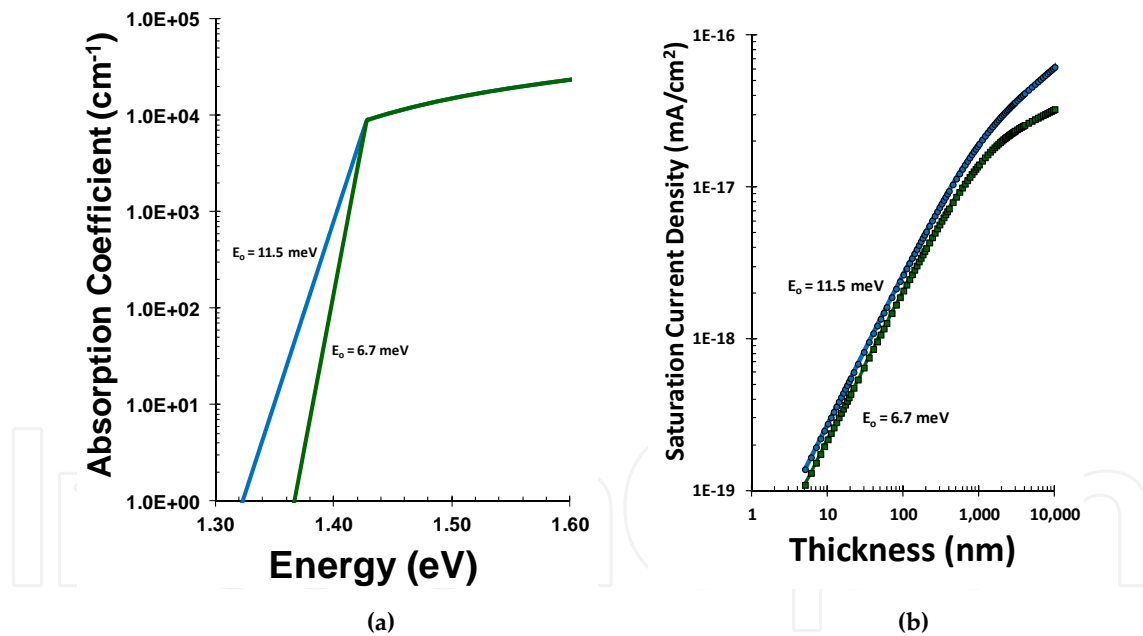

Figure 11. (a) Absorption spectra assuming two different activation energies (E_o) for the Urbach tail sub-band gap absorption, and (b) the resulting calculated radiative saturation current density as a function of absorber thickness.

Restricting the angular range of emissions provides another mechanism for reducing radiative dark current. The most direct means of restricting the range of angular emissions is to alter the refractive index environment in which the absorber layer is embedded. Figure 12 (a) summarizes the calculated radiative saturation dark current for several different refractive index values. Reducing the refractive index of the material above and below the absorber layer can
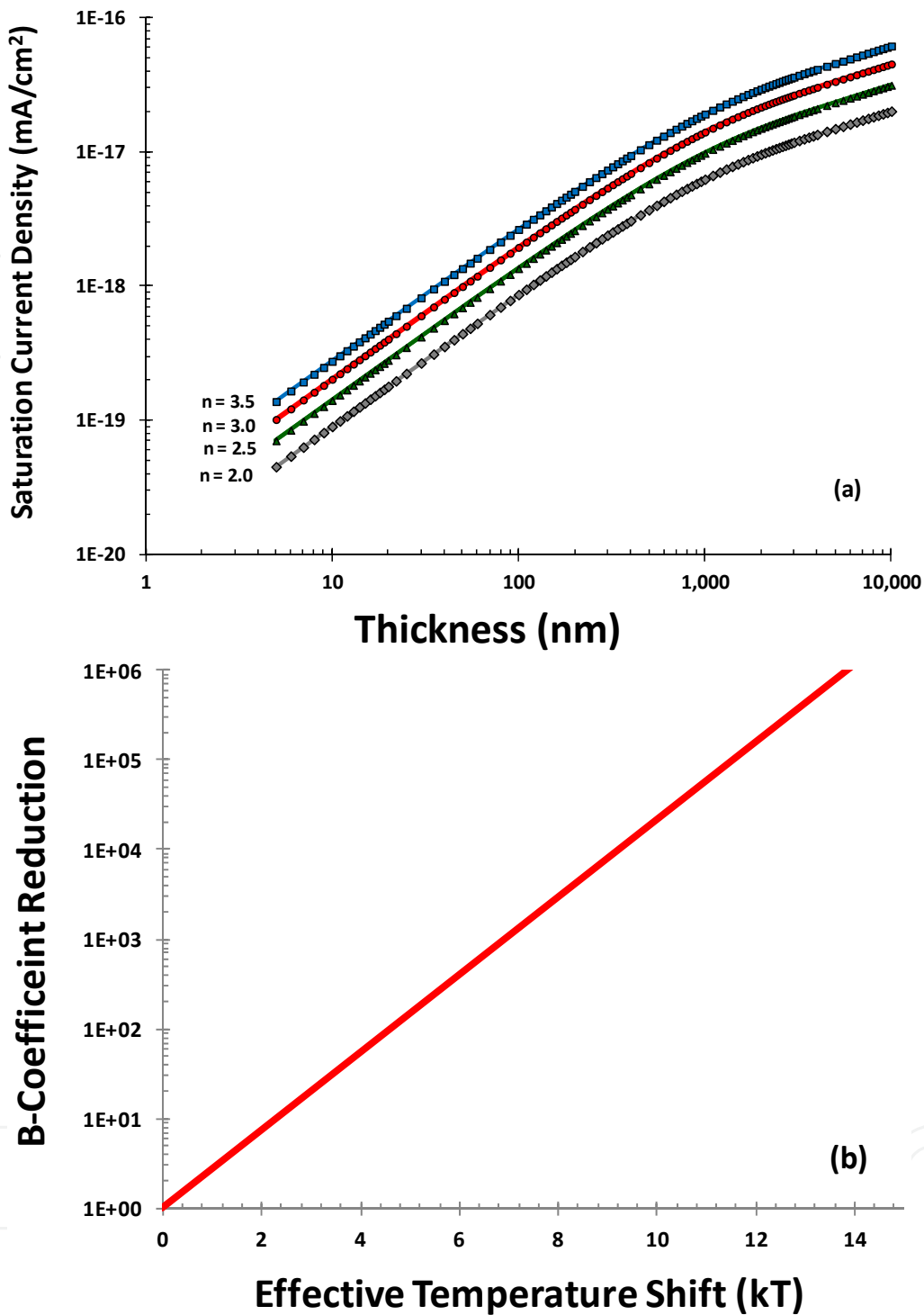
Figure 12. (a) Projected dependence of the radiative saturation dark current as a function of the refractive index of the material surrounding the absorber layer; and (b) Projected impact of hot carrier effects on the radiative recombination coefficient as a function of the effective carrier temperature difference between the barrier and wells.

effectively reduce the angular emissions, and lowering the refractive index from 3.5 to 2.5 can result in a 2x reduction in the radiative recombination coefficient. However, the changes in effective value of the refractive index in the step-graded structure are not expected to be this

large. Step-graded structures could also potentially alter the strain profile in the well, and strain in quantum wells has been found to result in a non-isotropic radiation profile that may reduce overall radiative recombination losses [31]. The non-isotropic radiation profile resulting from strain is in many ways similar to that resulting from a reduction in the refractive index of the barrier material, and while potentially beneficial, would seem unlikely to account for the 2x reduction in dark current observed in step-graded structures.

Step-graded structures may also provide a means of minimizing the overall recombination losses in quantum well solar cells. Faster escape rates can potentially be obtained by employing a step-graded compositional profile to allow photogenerated carriers to readily hop out of the InGaAs well [19], as illustrated in Figure 10. Enhanced extraction of hot carriers from the absorber region of a photovoltaic device has been suggested as a potential mechanism for reducing radiation losses and increasing efficiency [8]. Hot carrier effects can result in a large reduction in the radiative recombination, potentially reducing the B-coefficient by many orders of magnitude – see Figure 12 (b). Even a small effective carrier temperature difference of less than 1 kT is projected to result in more than a 2x reduction in the radiative dark current. Hot carrier effects can potentially be further enhanced by optimizing device design and employing optical concentration [8].

7. Intermediate band solar cells based on quantum dot nanostructures

In the previous section, we summarized how the operating voltage of nano-enhanced absorbers can be enhanced by suppressing the radiative dark current. In this section we will focus on the application of three dimensional quantum dot nanostructures in photovoltaics to increase the current output. Luque *et al.* [32] proposed that forming an intermediate band in a single junction photovoltaic cell can drastically enhance the energy conversion efficiency of the cell. The enhancement in efficiency is due to increased infrared light absorption via optical up-conversion. This type of internally up-converting PV device is known as an intermediate band solar cell (IBSC). Figure 13 shows the band diagram of a PV cell with an intermediate band. This configuration will enable the absorption of two additional sub-bandgap photons in addition to one above bandgap photon. With proper design, the ultimate open circuit voltage should not be affected by the insertion of the intermediate band. Instead, the open circuit voltage will be equal to the separation between valance and conduction band quasi Fermi levels of the wider bandgap host material, independent of the intermediate band material, i.e $V_{oc} = \mu_{CV}/q$. Based on the IBSC theory, a maximum efficiency is possible when the host material bandgap is 1.93 eV with an intermediate band located at 0.7 eV. Semiconductor quantum dots (QDs) are perhaps the best choice to create an intermediate band in a single-junction solar cell due to the inherent tunability of their shape, size, and quantum confinement properties. For an IBSC to work properly, the QD system being used must satisfy certain conditions in terms of bandgaps and band alignments [32].

Many attempts have been made to realize IBSCs based upon QD nanostructures. Initially, QD systems such as InAs, InGaAs, and GaSb dots with GaAs as host material have been studied.

InAs and InGaAs QDs in GaAs exhibit a type I band alignment, while GaSb QDs in GaAs have a type II band alignment. In type I QDs, both electrons in the conduction band and holes in the valence band are confined. In type II QDs, only one type of carriers is confined, for example, in GaSb QDs only holes are confined and electrons are delocalized. Compared to Type I QDs, Type II QD systems offer advantages with longer carrier life times. But in GaSb QDs the high effective mass of holes puts the hole energy levels close to each other and making it difficult to achieve an intermediate band. This makes InAs/GaAs system more appropriate to demonstrate the operation of IBSC. So far, QDs used for IBSC study have been grown using a self-assembly process known as the Stranski–Krastanov (S-K) growth method. Molecular beam epitaxy (MBE) and metal organic chemical vapor deposition (MOCVD) systems are generally used to synthesize such QDs. InAs QDs grown using on GaAs are typically 5-7 nm tall and 25-30 nm wide with QD density ranging from $10^{10} - 10^{11}$ cm^{-2}. Figure 14 shows the atomic force microscope (AFM) image of InAs QDs grown on GaAs and its distribution. The width of the intermediate band (ΔE_{IB}) formed by QD depends on the QD distribution. Larger QD distribution leads to higher ΔE_{IB}. Levy *et al*. calculated that highest cell efficiency results when $\Delta E_{IB} \sim$ 825 meV [33].
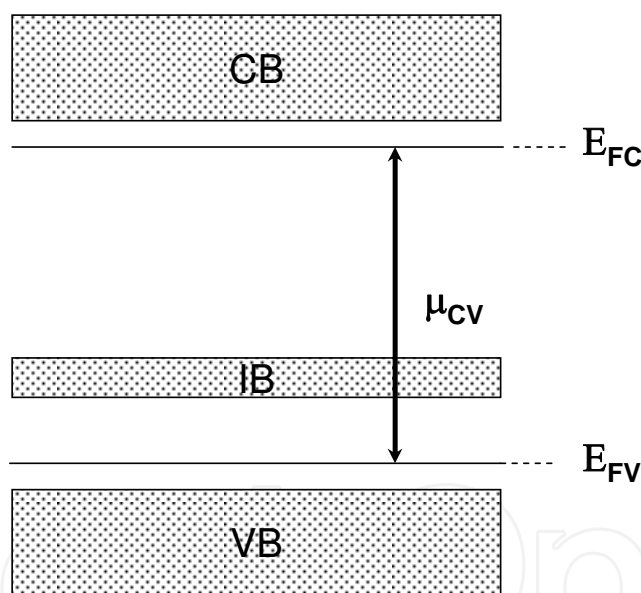

Figure 13. Schematic showing the bands involved in an intermediate band photovoltaic cell. The intermediate band is located between the conduction and valence bands of a barrier material. The open circuit voltage of this ideal cell is equal to the separation between the conduction and valence band quasi Fermi levels E_{FC} and E_{FV}. There are three transitions – valence band to conduction band, valence band to intermediate band, and intermediate band to conduction band – that contribute to the photocurrent.

A typical QD, due to its small size, has a small absorption cross section for incident photons. Due to this fact, a large number of QD layers need to be stacked together to provide sufficient sub-bandgap photon absorption. These layers are separated by a barrier material also known as a spacer. To accommodate a large number of dot layers in a given intrinsic region thickness, very thin spacers are used. However, the accumulated strain due to stacking the thin spacer

layers leads to the formation of defects and dislocations in the system. Figure 15 shows the high resolution TEM image of ten layers of InAs QDs on GaAs. A thin 15 nm spacer, which is not enough to de-couple strain between two successive dot layers, leads to dislocation formation. To avoid such effects due to QD stacking, a technique known as strain compensation has been adopted. In this technique, a tensile material with respect to both barrier and QD materials is inserted between two successive QD layers. GaP and GaAsN are widely used strain compensation materials for the InAs/GaAs system.

Figure 16 shows a schematic illustrating the strain compensation process in a multi-layer QD system. In order to compensate the strain accumulated during the stacking process, a material with smaller lattice constant with respect to the buffer layers is introduced between two successive QD layers. This process reduces the effects caused by the strain buildup. The strain compensation material and its thickness should be selected such that the total elastic strain in the system is less than a critical value. The total elastic strain (E_{total}) depends on the number of QD stacks (N), spacer thickness (t_{spacer}) and the average strain ($< \varepsilon_\perp >$) in each QD layer, i.e $E_{total} < N. t_{spacer.} < \varepsilon_\perp >$. For example, the use of a 4 monolayer (ML) thick GaP strain compensation layer relieves ~36% of the compressive strain in the InAs/GaAs material system [34]. To achieve good quality material, either the spacer should be thick enough so that the successive QD layers are strain de-coupled, or strain compensation layers must be employed. Strain compensation has been successfully implemented in photonic devices such as lasers and photovoltaic cells [29, 35-38].
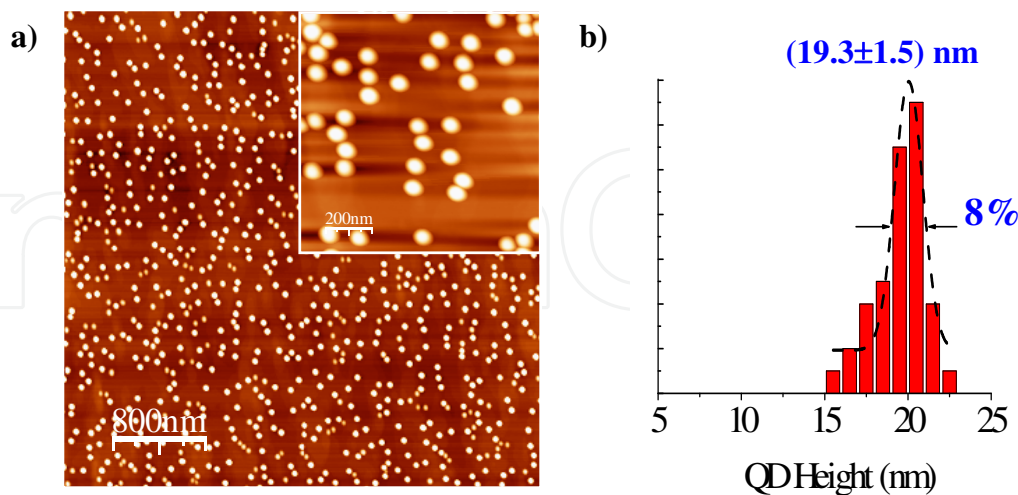

Figure 14. (a) Atomic force microscope image of InAs/GaAs QDs grown via the Stranski–Krastanov growth mode using MBE, and b) the resulting QD height distribution. As the formation of these QD is a strain driven process, a variation in QD size is expected. The FWHM of the distribution can be reduced with careful optimization of growth conditions.
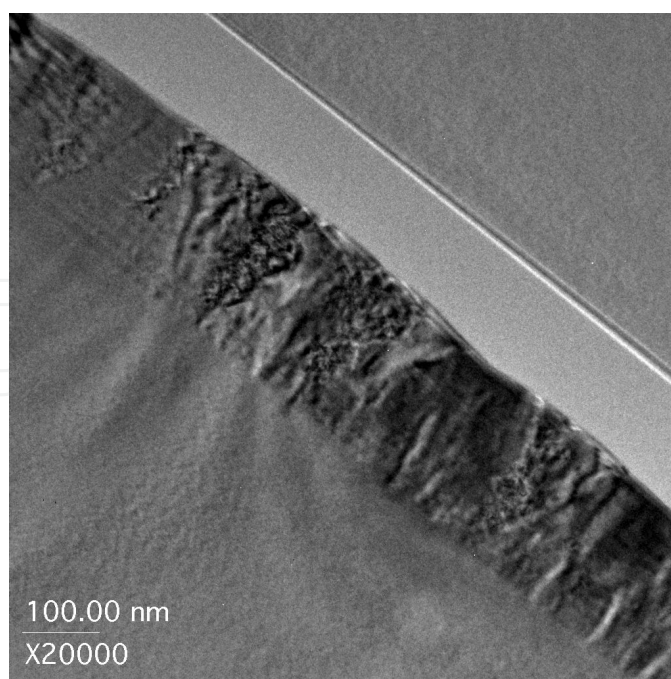
Figure 15. Cross-sectional TEM image of 10 stacks of InAs/GaAs QD grown by MOCVD with 15 nm spacers. In this structure, the use of thin spacer layers results in formation of unwanted dislocations [34].
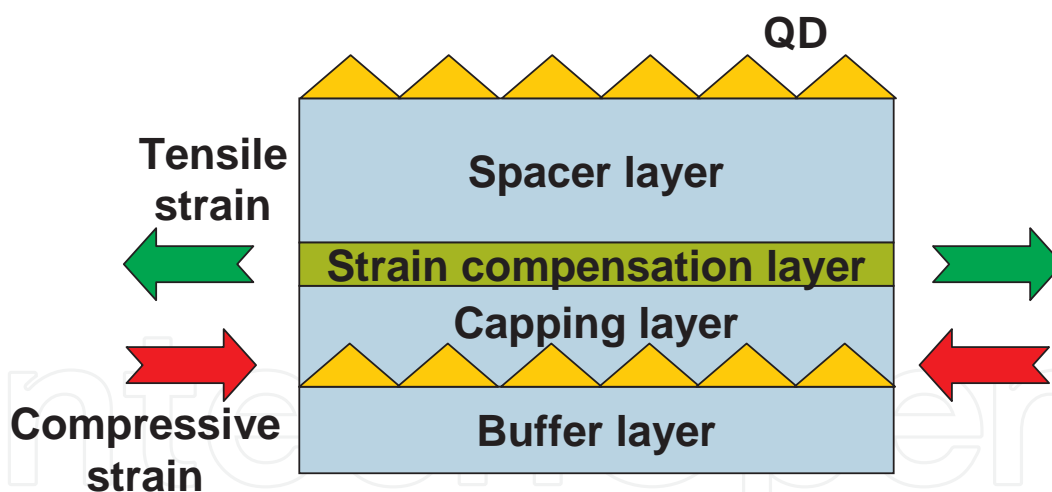

Figure 16. Schematic showing the implementation of strain compensation in a QD structure. Self-assembled QDs are formed due to compressive strain between QD and buffer materials. During the process of stacking QD layers, a material with smaller lattice constant (tensile with respect to buffer) is inserted between two successive QD layers to avoid strain induced effects.

Figure 17 shows a strain-compensated GaAs *p-i-n* photovoltaic cell in which 3 layers of InAs QD layers with a 29 nm GaAs spacer are inserted [38]. A 4 ML GaP strain compensation layer between two successive QD layers is also included here. One can easily study the affect of strain compensation by measuring PL from the stacked QD samples (transmission electron
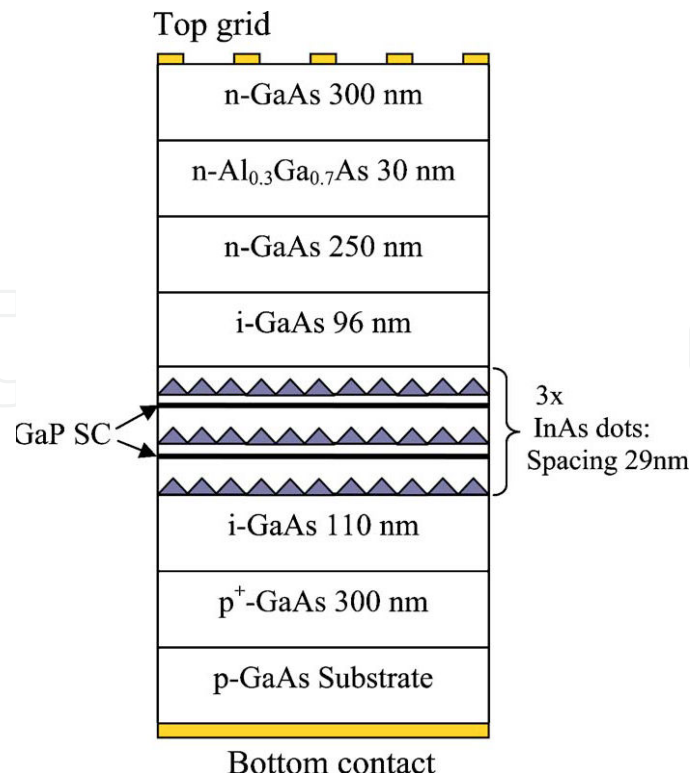
Figure 17. Schematic representation of an InAs/GaAs quantum dot photovoltaic device stucture with 3 QD layers that employ 4 ML GaP layers for strain compensation [38].

microscope and atomic force microscope also help in such study but are more destructive, expensive and time consuming). The PL measurements conducted on QDs alone are presented in Figure 18. The sample without GaP strain compensation has poor PL emission compared to that of the sample with strain compensation. This is indicative of poor material quality and increased defect density. PL from the sample without stain compensation also shows a bimodal distribution which indicates a large variation in dot size due to strain.

The electrical characteristics of QD photovoltaic cells with and without strain compensation have been studied via current-voltage (I-V) and quantum efficiency measurements. The I-V characteristics of InAs/GaAs QD PV cell structures (Figure 17) are compared in Figure 19. It is evident from the figure that the cell without strain compensation performs poorly when compared to other cells. In this study, three different GaP strain compensation schemes are chosen, i.e. 2 ML, 4 ML and 2ML+2ML (with 5 nm GaAs in between). It is observed from the data that both 4ML and 2ML+2ML samples behave in similar ways with the latter showing slightly better current. This observation is also supported by EQE data shown in Figure 20. The devices with QDs in their active regions show an extended photoresponse compared to the device without QDs. For a higher number of QD layers in the PV cell, a careful optimization of strain compensation layers is needed. Though this I-V data shows a drop in V_{OC} with the insertion of QDs in the PV cells, it is possible to develop QD cells with minimal voltage drop. Bailey *et al*. have demonstrated that by carefully tuning the QD and strain compensation material thicknesses, the V_{OC} can approach 1 V, comparable to that of the GaAs control cell [39].
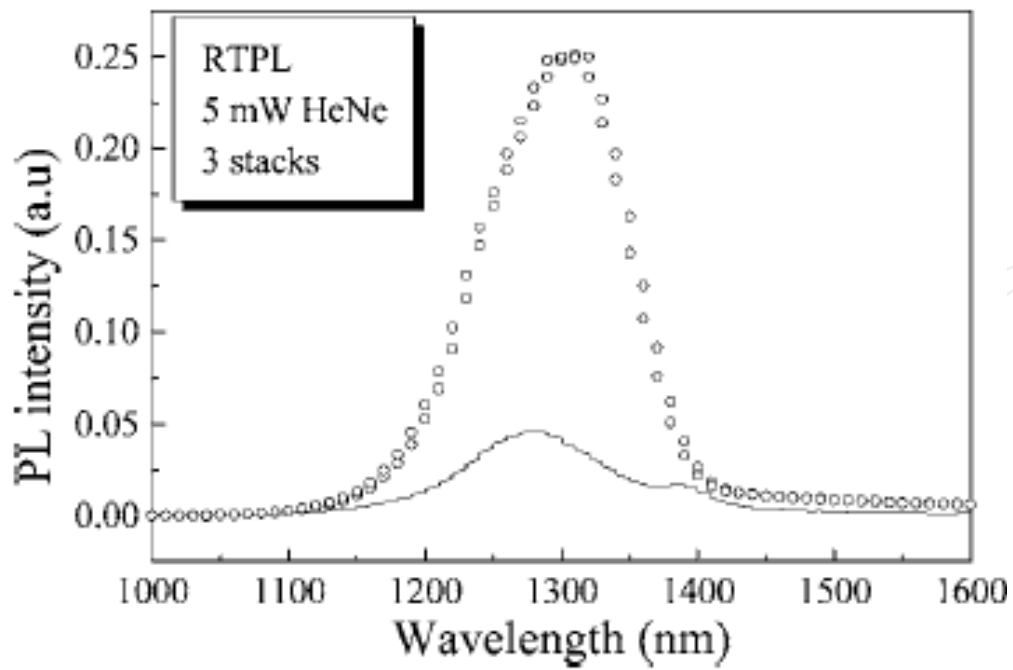
Figure 18. Photoluminescence spectra from 3 layers of stacked InAs QDs with (circles) and without (solid) strain compensation layers. It is obvious from these spectrums that including proper strain compensation layers improves the material quality.
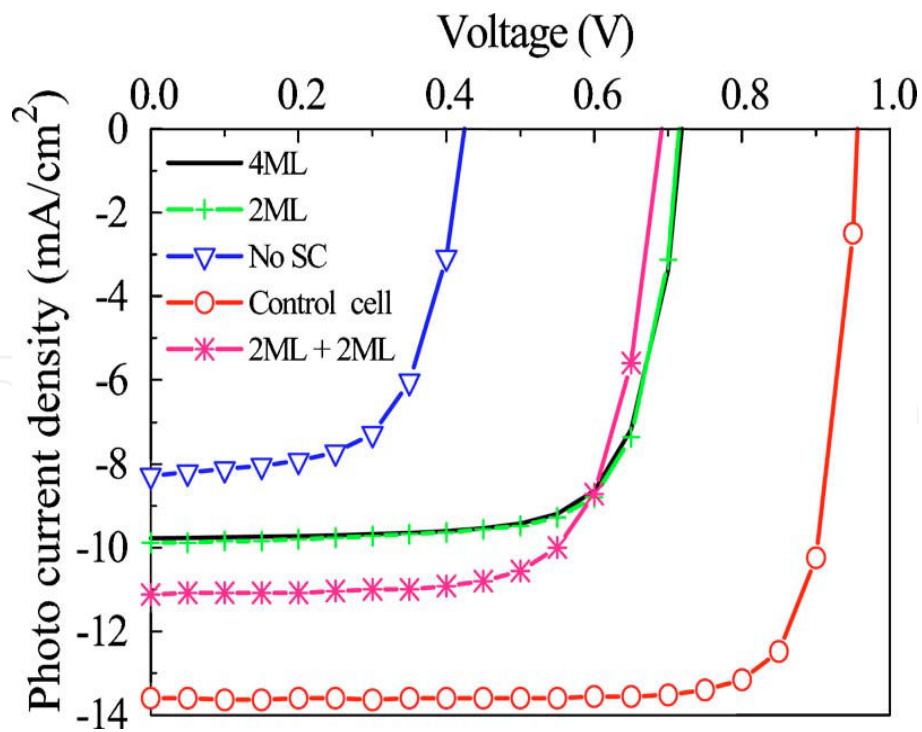

Figure 19. Current-voltage characteristics of InAs/GaAs QD photovoltaic cells with 3 QD layers. GaP has been used for compensating strain. A 2ML+2ML GaP with 5 ML separation provides best compensation.
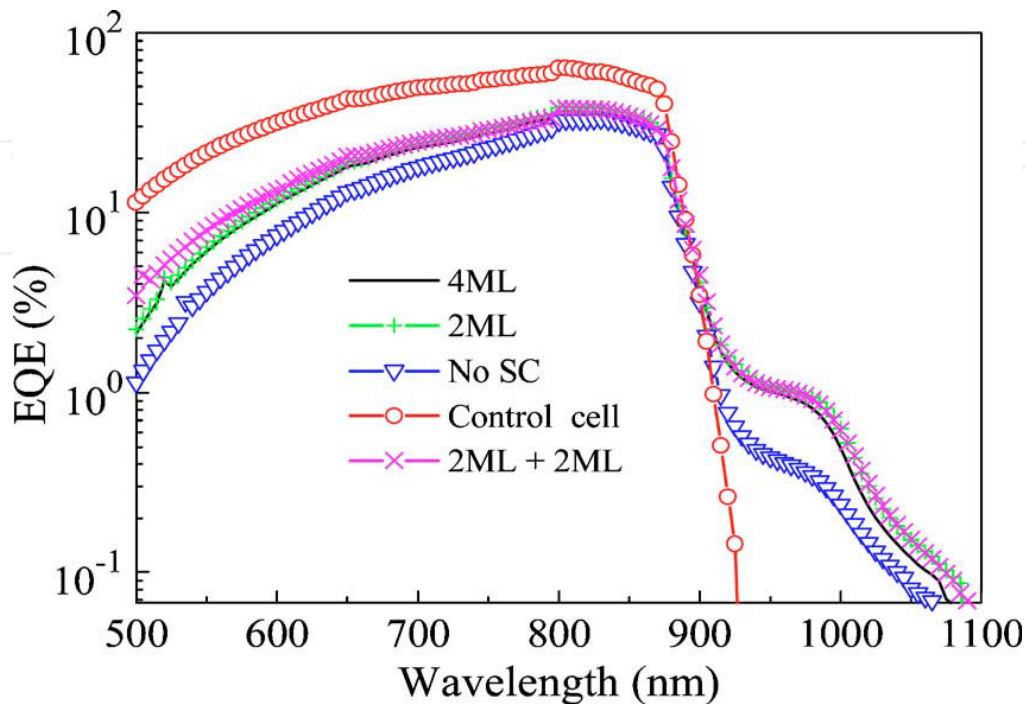
Figure 20. External quantum efficiency characteristics of photovoltaic cells fabricated with and without strain compensation layers. Clearly, the devices with strain compensation outperform the device without compensation.

8. Novel materials for intermediate band solar cells

As noted previously, there have been numerous attempts to use established QD material systems for IBSCs. However, these QD systems have had only limited success because their band alignments do not meet the IBSC requirements. Levy *et al.* and Dahal *et al.* have identified exotic material combinations that are more suitable for IBSCs [40, 41]. These material systems are difficult to grow and very few attempts have been made to realize them. Simmonds *et al.* have reported the growth of InAs(Sb) QDs with $AlAs_{0.56}Sb_{0.44}$ barriers on InP substrates [42]. This system has near ideal bandgaps for IBSCs, and furthermore, InAs(Sb)/AlAsSb QDs exhibit a type II band alignment. This offers strong electron confinement, while the valence band offset at the InAs(Sb)/AlAsSb interface is small (zero for certain As and Sb compositions). Initial attempts were made to develop InAs (no antimony) QDs. However, when InAs was directly grown on AlAsSb barriers, irrespective of good QD morphology, no PL emission was observed. This was attributed to aluminum diffusion into the QDs. The aluminum diffusion issue was solved by introducing very thin layers of $GaAs_xSb_{1-x}$ between the QD and AlAsSb layers. This process resulted in PL emission between 0.7 – 0.9 eV (at 77 K). The $GaAs_xSb_{1-x}$ spacer scheme was further optimized by Sun *et al.* to tune the QD morphology and bandgap [43].

Figure 21 (a) shows the schematic of InAs QD using GaAs and GaAsSb cladding layer scheme. Figure 21 (b) shows the atomic force microscope image of InAs/AlAsSb QDs with 5 ML of GaAs below the QDs. These QDs have an areal density 2×10^{10} cm^{-2} and are 4.1 nm tall and 33 nm in diameter. The average size of these QDs can be easily controlled, and hence the energies of the quantum confined states, simply by changing the InAs coverage. Power-dependent photoluminescence measurements on these QD samples confirm a type II band alignment (Figure 22). In samples containing GaAs/InAs/GaAsSb QDs, carrier lifetimes as long as 7 ns are measured. This is greater than the lifetimes measured in typical type I QD systems. These longer lifetimes are especially beneficial for efficient carrier extraction, leading to higher IBSC efficiency.
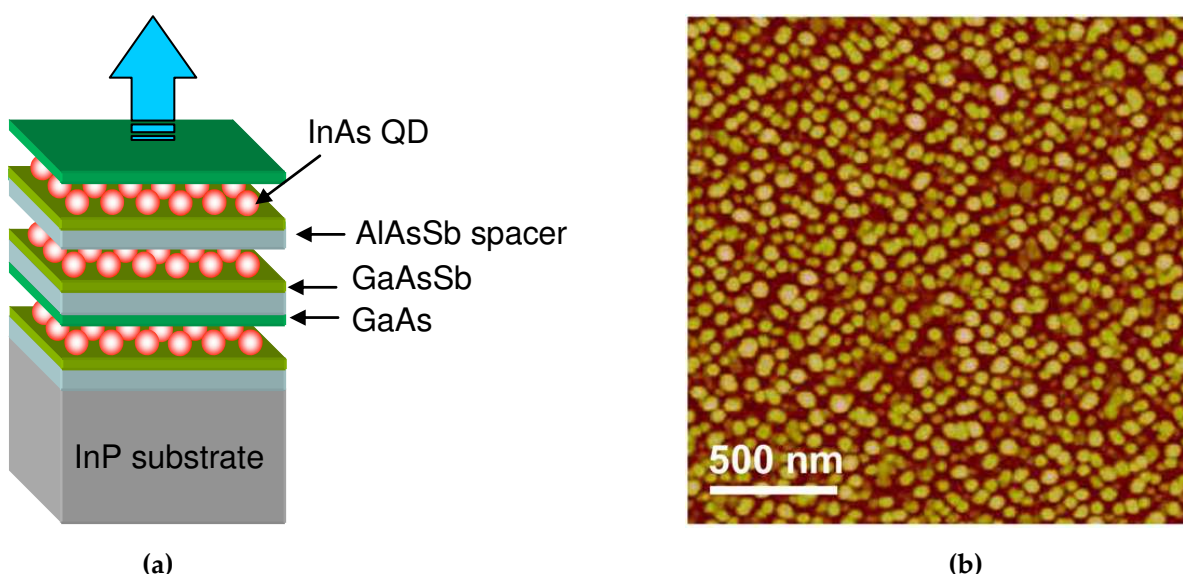

(a)   **(b)**

Figure 21. a) Schematic of an InAs QD structure with GaAs and GaAs$_{0.95}$Sb$_{0.05}$ cladding layers, as well as thin AlAsSb spacers, and b) atomic force microscopy image of InAs QDs on AlAs$_{0.56}$Sb$_{0.44}$ with a five-monolayer-thick GaAs cladding layer placed beneath the QDs. The QD density is 2×10^{10}cm^{-2}, and they are 4.1 nm tall and 33 nm in diameter [42].

To understand the performance and operation of InAs/AlAsSb QD PV cells, an AlAsSb p-i-n solar cell device was fabricated with 10 layers of InAs QDs buried within the optimized cladding layers (similar to schematic in Figure 21(a)). EQE data from an AlAsSb control cell without dots or cladding layers and another cell with cladding layers only is also presented for comparison (Figure 23). The EQE spectra show an extended wavelength response in cases where there are cladding layers and QDs. To date, this is the longest wavelength response reported in any QD PV device. The QD cell shows an extremely broad-band photoresponse up to 1800 nm, consistent with the PL measured from respective devices. Though these results are encouraging, further device optimization will be required to achieve a high efficiency IBSC performance, perhaps including the use of high solar concentrations.
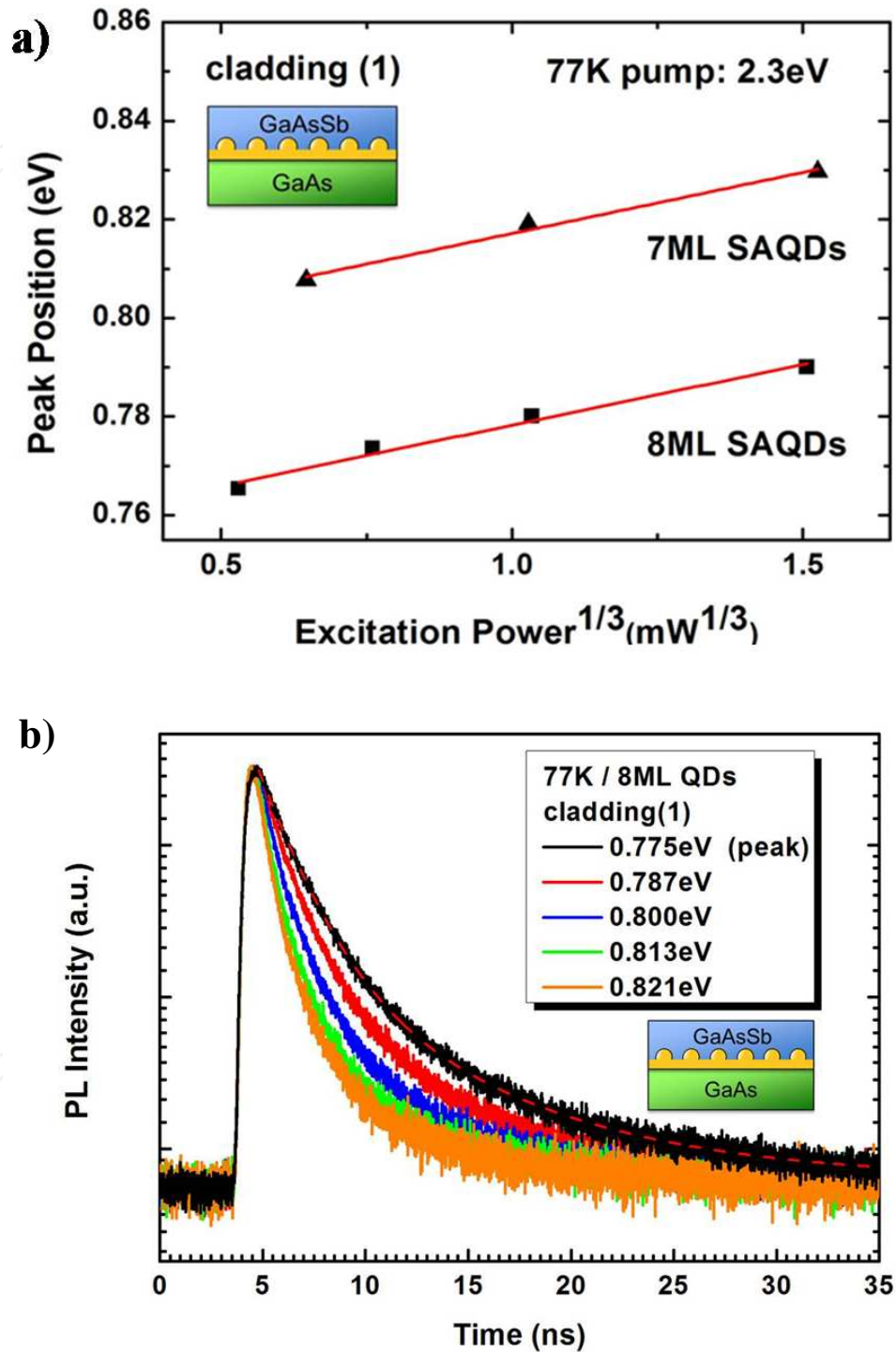
Figure 22. (a) PL peak position at 77 K as a function of the cube root of excitation power for 7 ML and 8 ML InAs QDs with optimized cladding scheme, shown in the inset, and b) time dependent PL decay traces for 8 ML InAs SAQDs at different detection wavelengths. The dashed line is the fitting curve for the decay trace at peak wavelength.
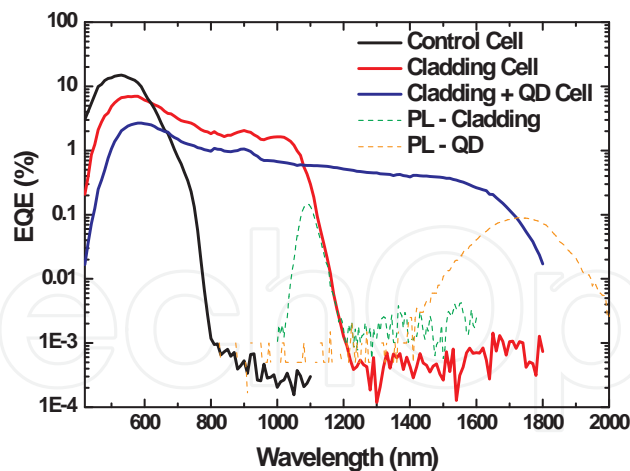
Figure 23. External quantum efficiency measured from an InAs/AlAsSb QD PV cell with GaAs and GaAsSb cladding layers, compared to measurements from a control cell and a cell incorporating only the cladding layers (no QDs). The QD cell shows a response up to 1800 nm, consistent with the PL measurements.

9. Conclusions

While multi-junction III-V devices have achieved record-breaking efficiency under select operating conditions, inherent sensitivity to changes in the spectral conditions and high manufacturing costs preclude their wide-spread usage in energy harvesting applications. On the other hand, thin-film single-junction III-V devices can offer more robust performance at lower costs. Moreover, single-junction III-V cells can potentially match or even exceed the peak efficiency performance levels of present day multi-junction devices by incorporating advanced structures that leverage light trapping, optical up-conversion and/or hot carrier effects.

In this chapter, the theoretical performance of optically-thin solar cells has been described using a generalized detailed balance model, specifically adapted for nano-enhanced absorbers. This model has been employed to assess the impact of both absorber thickness and effective optical path length on the performance of III-V photovoltaic devices, using data from GaAs-based structures to validate the approach. In later sections, recent experimental work focused on reducing the diode dark current (and hence increasing the operating voltage) and boosting the current output of nano-enhanced III-V solar cells has been summarized. In particular, the combination of a thin optical absorber and advanced light trapping structures was shown to provide a means to increase the voltage of operation while maintaining current output in photovoltaic devices. However, if the absorber thickness is reduced too far, two-dimensional carrier confinement will effectively enhance radiative recombination and negate the voltage benefits of thin-absorber cells. In addition, optical losses in the high-doped contact layers and surface regions can limit some of the enhanced voltage benefits of light-trapping in thin absorber structures. There are, however, several other mechanisms for reducing radiative emissions in photovoltaic devices. For example, radiative emissions can be minimized and the voltage increased by embedding thin-absorbers in lower refractive index material or employ-

ing step-graded structures to harness hot carrier effects. Finally, infrared up-conversion has been demonstrated as a pathway to enhance current output in intermediate band solar cells.

Author details

Roger E. Welser[1], Ashok K. Sood[1*], Ramesh B. Laghumavarapu[2], Diana L. Huffaker[2], David M. Wilt[3], Nibir K. Dhar[4] and Kimberly A. Sablon[5]

*Address all correspondence to: aksood@magnoliaoptical.com

1 Magnolia Solar, Inc., 251 Fuller Road, CESTM-B250, Albany, NY, USA

2 Electrical Engineering Department, University of California Los Angeles, CA, USA

3 Space Vehicle Directorate, Air Force Research Laboratory, Kirtland AFB, NM, USA

4 DARPA/MTO, 675 North Randolph Street, Arlington, VA, USA

5 Army Research Laboratory, 2800 Powder Mill Road, Adelphi, MD, USA

References

[1] A. Chirilă, S. Buecheler, F. Pianezzi, P. Bloesch, C. Gretener, A. R. Uhl, C. Fella, L. Kranz, J. Perrenoud, S. Seyrling, R. Verma, S. Nishiwaki, Y. E. Romanyuk, G. Bilger, and A. N. Tiwari, "Highly Efficient Cu(In,Ga)Se$_2$ Solar Cells Grown on Flexible Polymer Films," *Nature Materials*, vol. 10, pp. 857-861 (September 2011).

[2] C. Youtsey, J. Adams, R. Chan, V. Elarde, G. Hillier, M. Osowski, D. McCallum, H. Miyamoto, N. Pan, C. Stender, R. Tatavarti, F. Tuminello, A. Wibowo, "Epitaxial Lift-Off of Large-Area GaAs Thin-Film Multi-Junction Solar Cells," Proc. of the CS MAN-TECH Conference (April 2012).

[3] P. Patel, D. Aiken, A. Boca, B. Cho, D. Chumney, M. B. Clevenger, A. Cornfeld, N. Fatemi, Y. Lin, J. McCarty, F. Newman, P. Sharps, J. Spann, M. Stan, J. Steinfeldt, C. Strautin, and T. Varghese, "Experimental Results From Performance Improvement and Radiation Hardening of Inverted Metamorphic Multijunction Solar Cells," IEEE J. of Photovoltaics 2, 377 - 381 (July 2012).

[4] J. Boisvert, D. Law, R. King, E. Rehder, P. Chiu, D. Bhusari, C. Fetzer, X. Liu, W. Hong S. Mesropian, R. Woo, K. Edmondson, H. Cotal, D. Krut, S. Singer, S. Wierman, and N. H. Karam, "High Efficiency Inverted Metamorphic (IMM) Solar Cells," Proceedings of 39th IEEE PVSC Conference, Tampa, pp. 2790 - 2792 (June 2013).

[5] http://www.nrel.gov/ncpv/images/efficiency_chart.jpg

[6] R. E. Welser, G. G. Pethuraja, J. W. Zeller, A. K. Sood, K. A. Sablon, S. R. Tatavarti, and N. K. Dhar, "High-Voltage Thin-Absorber Photovoltaic Device Structures For Efficient Energy Harvesting," Proc. of SPIE, vol. 9115, no. 9115-14 (May 2014).

[7] T. Trupke and P. Wurfel, "Improved Spectral Response of Triple Tandem Solar Cells by Combined Series / Parallel Interconnection," J. Applied Phys., vol. 96, pp. 2347-2351 (August 2004).

[8] L. C. Hirst, H. Fujii, Y. Wang, M. Sygiyama, and N. J. Ekins-Daukes, "Hot Carriers in Quantum Wells for Photovoltaic Efficiency Enhancement," IEEE J. of Photovoltaics 4, 244-252 (January 2014).

[9] W. Shockley and H. J. Queisser, "Detailed Balance Limit of Efficiency of p-n Junction Solar Cells," J. Appl. Phys. 32, 510-519 (March 1961).

[10] T. Tiedje, E. Yablonovitch, G. D. Cody, and B. G. Brooks, "Limiting Efficiency of Silicon Solar Cells," IEEE Trans. Electron Devices 31, 711-716 (May 1984).

[11] A. Marti, J. L. Balenzategui, and R. F. Reyna, "Photon Recycling and Shockley's Diode Equation," J. Appl. Phys. 82, 4067-4075 (June 1997).

[12] U. Rau, "Reciprocity Relation Between Photovoltaic Quantum Efficiency and Electroluminescence Emission of Solar Cells," Phys. Rev. B 76, 085303 (August 2007).

[13] T. Kirchartz and U. Rau, "Electroluminescence Analysis of High Efficiency Cu(In,Ga)Se$_2$ Solar Cells," J. Appl. Phys. 102, 104510 (November 2007).

[14] S. Roensch, R. Hoheisel, F. Dimroth, and A. W. Bett, "Subcell I-V Characteristic Analysis of GaInP/GaInAs/Ge Solar Cells Using Electroluminescence Measurements," Appl. Phys. Lett. 98, 251113 (June 2011).

[15] T. Trupke, M. A. Green, and P. Wurfel, "Improving Solar Cell Efficiencies by Up-Conversion of Sub-Band-Gap Light," J. Appl. Phys. 92, 4117-4122 (October 2002).

[16] K. A. Sablon, J. W. Little, V. Mitin, A. Sergeev, N. Vagidov, and K. Reinhardt, "Strong Enhancement of Solar Cell Efficiency Due to Quantum Dots with Built-In Charge," Nano Lett. 11, 2311-2317 (May 2011).

[17] M. Sugiyama, Y. Wang, K. Watanabe, T. Morioka, Y. Okada, and Y. Nakano, "Photocurrent Generation by Two-Step Photon Absorption with Quantum-Well Superlattice Cell," IEEE J. Photovoltaics 2, 298-302 (July 2012).

[18] R. B. Laghumavarapu, M. Sun, P. J. Simmonds, B. Liang, S. Hellstroem, Z. Bittner, S. Polly, S. Hubbard, A. G. Norman, J-W. Luo, R. Welser, A. K. Sood, and D. L. Huffaker, "New Quantum Dot Nanomaterials to Boost Solar Energy Harvesting," SPIE Newsroom 10.1117/2.1201401.005315 (January 2014).

[19] R. E. Welser, O. A. Laboutin, M. Chaplin, and V. Un, "Reducing Non-Radiative and Radiative Recombination in InGaAs Quantum Well Solar Cells," Proceedings of the 37th IEEE Photovoltaic Specialists Conference, 002683-002686 (June 2011).

[20] R. Tatavarti, A. Wibowo, G. Martin, F. Tuminello, C. Youtsey, G. Hillier, N. Pan, M.W. Wanlass, and M. Romero, "InGaP/ GaAs / InGaAs Inverted Metamorphic Solar Cells on 4" Epitaxial Lifted Off (ELO) Wafers," Proceedings of 35th IEEE PVSC conference, Honolulu, pp. 002125 - 002128 (June 2010).

[21] O. D. Miller, E. Yablonovitch, and S. R. Kurtz, "Strong Internal and External Luminescence as Solar Cells Approach the Shockley-Queisser Limit," *IEEE J. of Photovoltaics*, vol. 2, pp. 303-311 (July 2012).

[22] S. Kurtz, J. F. Geisz, D. J. Friedman, J. M. Olson, and A. Duda, "Modeling of Electron Diffusion Length in GaInAsN Solar Cells," Proceedings of the 28th IEEE Photovoltaic Specialists Conference, pp. 1210-1212 (September 2000).

[23] G. B. Lush, "B-coefficient in n-type GaAs," *Solar Energy Materials & Solar Cells*, vol. 93, pp. 1225-1229 (March 2009).

[24] P. Asbeck, "Self-Absorption Effects on the Radiative Lifetime in GaAs-GaAlAs Double Heterostructures," *J. Appl. Phys.*, vol. 48, pp. 820-822 (February 1977).

[25] A. Alemu, J. A. H. Coaquira, and A. Freundlich, "Dependence of Device Performance on Carrier Escape Sequence in Multi-Quantum-Well p-i-n Solar Cells," J. Appl. Phys. 99, 084506 (May 2006).

[26] P. Blood, "On the Dimensionality of Optical Absorption, Gain, and Recombination in Quantum-Confined Structures," IEEE J. of Quantum Electronics 36, 354-362 (March 2000).

[27] K. W. J. Barnham and G. Duggan, "A New Approach to High-Efficiency Multi-Band-Gap Solar Cells," J. Appl. Phys. 67, 3490-3493 (April 1990).

[28] R. B. Laghumavarapu, A. Moscho, A. Khoshakhlagh, M. El-Emawy, L.F. Lester, and D.L. Huffaker, "GaSb/GaAs Type II Quantum Dot Solar Cells for Enhanced Infrared Spectral Response," Appl. Phys. Lett. 90, 173125 (April 2007).

[29] S. M. Hubbard, C. D. Cress, C. G. Bailey, R. P. Raffaelle, S. G. Bailey, D. M. Wilt, "Effect of Strain Compensation on Quantum Dot Enhanced GaAs Solar Cells," Appl. Phys. Lett. 92, p. 123512, (March 2008).

[30] R. E. Welser, "Thick-Well Quantum-Structured Solar Cells: Design Criteria for Nano-Enhanced Absorbers," Proc. of SPIE, vol. 8620, no. 86201C (February 2013).

[31] J. G. J. Adams, W. Elder, G. Hill, J. S. Roberts, K. W. J. Barnham and N. J. Ekins-Daukes, "Higher Limiting Efficiencies for Nanostructured Solar Cells," Proc. of SPIE Vol. 7597, 759705 (January 2010).

[32] A. Luque and A. Marti, "Increasing the Efficiency of Ideal Solar Cells by Photon In-duced Transitions at Intermediate Levels," Phys. Rev. Lett., vol. 76, pp. 5014-5017 (June 1997)

[33] M. Y. Levy, and C. Honsberg, "Solar cell with an intermediate band of finite width," Physical Review B, 78(16), 165122 (2008).

[34] N. Nuntawong, "Strain Compensation Technique in InAs/GaAs SAQD Structure Grown by Metalorganic Chemical Vapor Deposition," Ph.D. Dissertation, University of New Mexico (2007).

[35] A. Kouichi, N. Yamamoto, and M. Tsuchiya. "Highly Stacked Quantum-Dot Laser Fabricated Using a Strain Compensation Technique," Appl. Phys. Lett., 93(4) 041121 (2008).

[36] N. Nuntawong, Y. C.Xin, S. Birudavolu, P. S. Wong, S. Huang, C. P Hains, and D. L. Huffaker, "Quantum Dot Lasers Based on a Stacked and Strain-Compensated Active Region Grown by Metal-Organic Chemical Vapor Deposition," Appl. Phys. Lett., 86(19), 193115-193115 (2005).

[37] R. Oshima, A. Takata, Y. Okada, "Strain-Compensated InAs/GaNAs Quantum Dots for Use in High-Efficiency Solar Cells," Appl. Phys. Lett. 93, 083111, (2008).

[38] R. B. Laghumavarapu, M. El-Emawy, N. Nuntawong, A. Moscho, L. F. Lester, and D. L. Huffaker. "Improved device performance of InAs/GaAs quantum dot solar cells with GaP strain compensation layers," Appl. Phys. Lett. 91, no. 24 243115-243115 (2007).

[39] C. G. Bailey, D. V. Forbes, R. P. Raffaelle, and S. M. Hubbard, "Near 1V open circuit voltage InAs/GaAs quantum dot solar cells", Appl. Phys. Lett., 98(16), 163105 (2011).

[40] M. Y. Levy, C. Honsberg, A. Martí, and A. Luque, "Quantum Dot Intermediate Band Solar Cell Material Systems with Negligible Valence Band Offsets," IEEE 31st Photo-voltaic Specialists Conference, pp. 90-93 (2005).

[41] S. N. Dahal, S. P. Bremner, and C. B. Honsberg, "Band Structure Calculation for Quantum Dot Solar Cells using KP Method," IEEE 33rd Photovoltaic Specialists Con-ference, pp. 1-4, (2008).

[42] P. J. Simmonds, R. B. Laghumavarapu, M. Sun, A. Lin, C. J. Reyner, B. Liang, and D. L. Huffaker, "Structural and Optical Properties of InAs/AlAsSb Quantum Dots with GaAs (Sb) Cladding Layers," Appl. Phys. Lett. 100(24), 243108 (2012).

[43] M. Sun, P. J. Simmonds, R. B. Laghumavarapu, A. Lin, C. J. Reyner, H.-S. Duan, B. Liang, D. L. Huffaker, "Effects of GaAs(Sb) Cladding Layers on InAs/AlAsSb Quan-tum Dots," Appl. Phys. Lett. 102, p. 023107 (2013).